

**Searches for new physics
in $t\bar{t}$ pair production
at the Large Hadron Collider**

Candidate

Antonella Succurro

Supervised by

Dr. Aurelio Juste Rozas

Institució Catalana de Recerca i Estudis Avancat

Institut de Física d'Altes Energies

Professore: Lei ha una qualche ambizione?

Nicola: Ma... Non...

Professore: E Allora vada via... Se ne vada dall'Italia. Lasci l'Italia finché è in tempo.
Cosa vuole fare, il chirurgo?

Nicola: Non lo so, non ho ancora deciso...

Professore: Qualsiasi cosa decida, vada a studiare a Londra, a Parigi... Vada in
America, se ha le possibilità, ma lasci questo Paese. L'Italia è un Paese da
distruggere: un posto bello e inutile, destinato a morire.

Nicola: Cioè, secondo lei tra poco ci sarà un'apocalisse?

Professore: E magari ci fosse, almeno saremmo tutti costretti a ricostruire... Invece
qui rimane tutto immobile, uguale, in mano ai dinosauri. Dia retta, vada via...

da La meglio Gioventù di M.T. Giordana (2003)

⁴ Introduccion

⁵

Contents

8	Introduction	ix
9	1 Going beyond the Standard Model	1
10	1.1 Building the Standard Model	1
11	1.2 New Physics Models predicting vector-like quarks	1
12	2 The ATLAS experiment at the Large Hadron Collider	3
13	2.1 The Large Hadron Collider at CERN	3
14	2.2 The ATLAS detector	7
15	2.2.1 Coordinate system	8
16	2.2.2 Magnets	10
17	2.2.3 Inner detector	10
18	2.2.4 Calorimeters	13
19	2.2.5 Muon spectrometer	17
20	2.3 Forward sub-detectors	18
21	2.4 Trigger system	19
22	2.4.1 Level 1 trigger	20
23	2.4.2 Level 2 trigger	21
24	2.4.3 Event filter	21
25	2.5 Data Quality	21
26	3 Monte Carlo simulation	23
27	3.1 Phenomenology of p-p collisions	23
28	3.1.1 Proton structure	24
29	3.1.2 Factorization theorem	25
30	3.2 Simulation of p-p collisions	26
31	3.2.1 Hard interaction	26
32	3.2.2 Parton shower	28
33	3.2.3 Hadronization	31

34	3.2.4 Underlying event	32
35	3.3 Generators	33
36	3.4 ATLAS detector simulation	35
37	3.5 Monte Carlo samples corrections	35
38	4 Event reconstruction	37
39	4.1 ID Tracks	37
40	4.2 Primary vertices	38
41	4.3 Energy clusters	39
42	4.4 Electrons	40
43	4.5 Muons	42
44	4.6 Jets	44
45	4.6.2 b -tagging	46
46	4.7 Missing Transverse Energy	48
47	5 Searches for vector-like top partner pairs in the single lepton channel	51
48	5.1 General strategy for vector-like quark pairs searches	51
49	5.2 Data sample and common event preselection	54
50	5.3 Background and signal modeling	55
51	5.3.1 Monte Carlo simulated samples	56
52	5.3.2 Multi-jet background	58
53	5.4 Systematical uncertainties treatment	60
54	6 Preliminary search for $T\bar{T}$ pairs decaying to $Wb + X$	61
55	6.1 Boosted W reconstruction	61
56	6.2 Control regions	61
57	6.3 Event selection	61
58	6.4 Systematics	61
59	7 Preliminary search for $T\bar{T}$ pairs decaying to $Ht + X$	63
60	7.1 Control regions	63
61	7.2 Event selection	63
62	7.3 Systematics	63
63	8 Results	65
64	8.1 Combination	65
65	Conclusions	67
66	A Multi-jet background estimation in the single muon plus jets channel	69
67	B	75
68	C Search for $T\bar{T} \rightarrow Wb + X$ at $\sqrt{7}$ TeV	77
69	Bibliography	79

70 Introduction

71

72 The analyses presented in this dissertation have been performed analyzing data from
73 proton-proton (p-p) collisions at the center of mass energy $\sqrt{s} = 8$ TeV recorded during the
74 year 2012 at the ATLAS experiment [\[1\]](#).

76 Going beyond the Standard Model

77

78 The Standard Model (SM) of particle physics is the most successful, beautiful and
79 precise theory describing the interactions between fundamental particles. Its validity has
80 been tested by precision measurements at the Large Electron-Positron Collider (LEP) at
81 CERN and confirmed by the observation of all the particles it predicts, including the Higgs-
82 like boson discovered at the Large Hadron Collider (LHC) in July of 2012 which up to now
83 behaves as expected from the SM.

84 What makes the SM “only” and effective theory is the fact that unstabilities appear at
85 high energy scales of the order of the Planck mass. In this Chapter we will show

86 1.1 Building the Standard Model

87 1.2 New Physics Models predicting vector-like quarks

88 [2, 3]

The ATLAS experiment at the Large Hadron Collider

The time when particle physics experiments could fit in one's loft is well passed, if it ever existed. The reason is simple, as the deeper we want to investigate matter, the highest the energy we need. According to the Standard Model, we now know all the particles composing ordinary matter present in nature, so if we want to see something new, we need to produce it. The way to do it is suggested by one of the fundamental principles of relativity, $E = mc^2$, according to which we can smash massive particles and observe what other kind of matter comes out of the available energy. Soon enough after the discovery of the muon, after observing all the observable from cosmic rays, physicists started to do that using particle accelerators, the last of them in history being the Large Hadron Collider.

The Large Hadron Collider, built to collide protons at a center of mass energy of 14 TeV, is the world's highest energy particle accelerator, overcoming the Tevatron proton-antiproton collider where the top quark was discovered in 1995 [4, 5]. The ATLAS experiment is one of the collaborations that take advantage of the collisions provided by the Large Hadron Collider, and has been conceived to pursue a challenging physics program with, at the head of the list, the discovery of the Higgs boson, achieved in 2012 [6].

In the following Chapter we will briefly describe the main features of the accelerator and with some more details the ATLAS detector, both located at the CERN laboratories in Geneva, Switzerland.

2.1 The Large Hadron Collider at CERN

The LHC program was approved by CERN Council in 1994, followed by the approval of the four main experiments: ATLAS [1] and CMS [7] in 1996; ALICE [8] in 1997; LHCb [9] in 1998. Works towards the installation of the most powerful particle accelerator of the world started when the Large Electron Positron Collider (LEP) was dismantled in 2000 to give up its place in the tunnel to the LHC, which was then fully operational by 2008.

The ATLAS experiment [1] is situated at Point 1 along the Large Hadron Collider

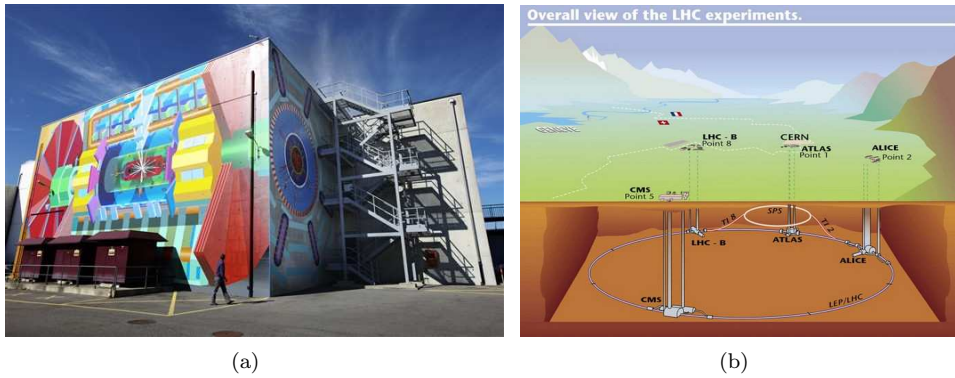


Figure 2.1: Left: View of Point 1, just above the ATLAS cavern, with a mural painting of the detector, reproduced at a scale of about 1:3 by artist Josef Kristofletti¹. Right: A drawing of the LHC complex.

(LHC) [10] 27 km long ring (Figure 2.1). The accelerator tunnel can reach an underground depth of 175 meters and is spread between Swiss and French territory, while the cave where ATLAS is allocated is about 100 meters underground in the CERN Swiss site of Meyrin.

The collider accelerates protons up to 4 TeV, but is designed to reach 7 TeV per beam when it will be operated at his full potential. This energy is achieved through various steps, shown in Figure 2.2. To start with, protons are extracted from Hydrogen gas and injected in the first machine, the linear accelerator LINAC2 that starts the acceleration chain. When protons reach an energy of 50 MeV they are injected into the Proton Synchrotron Booster (PSB) and accelerated up to the energy of 1.4 GeV. The second circular accelerator, the Proton Synchrotron (PS) brings the energy of the protons to 25 GeV previous to injecting them into the last machine before the LHC, the Super Proton Synchrotron (SPS). Protons of 450 GeV finally enter the LHC where they are boosted to energies of up to 4 TeV. The four main LHC experiments are shown on the collider ring.

The LHC is composed of eight arcs 2.7 km long, each of which contains 154 dipole magnets, whose function is to bend the beams along the circular trajectory, and 49 quadrupole magnets, that focus the beam. These superconducting magnets operate at a temperature of 1.9 K, maintained by means of liquid Helium vessels. Eight insertions are placed inbetween the arches. Each insertion has a specific role that characterizes its design and can be injection, beam dumping, beam cleaning, or “physics”, i.e. make the beams collide within an experiment.

First proton beams were circulated on 10th September 2008 and right on the verge of getting the first collisions at a center of mass energy $\sqrt{s} = 900$ GeV nine days later, an electrical connection joining superconducting wires of a dipole and a quadrupole failed. This caused the release of liquid Helium in the insulating vacuum, resulting in an explosion that severely damaged the machine. After more than one year devoted to repair the damage and consolidate the security, on 30th November 2009 the LHC became the world’s highest energy particle accelerator²:

¹More info at: <http://www.atlas.ch/mural/>.

²<http://press.web.cern.ch/press/PressReleases/Releases2009/PR18.09E.html>

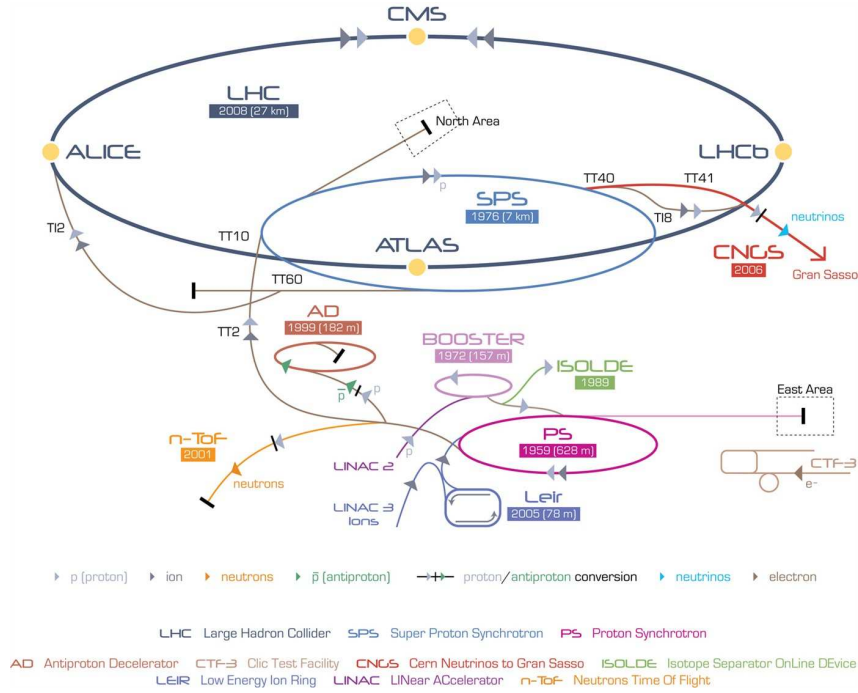


Figure 2.2: A schematic showing the accelerator complex at CERN.

145 Geneva, 30 November 2009. CERN's Large Hadron Collider has today become the
 146 world's highest energy particle accelerator, having accelerated its twin beams of protons
 147 to an energy of 1.18 TeV in the early hours of the morning. This exceeds the previous
 148 world record of 0.98 TeV, which had been held by the US Fermi National Accelerator
 149 Laboratory's Tevatron collider since 2001. It marks another important milestone on the
 150 road to first physics at the LHC in 2010.

One of the main characteristics for an accelerator is the luminosity, the instantaneous luminosity \mathcal{L} being defined as

$$\mathcal{L} \times \sigma = \frac{dN}{dt} = f \times n \frac{N_1 \times N_2}{A} \times \sigma. \quad (2.1)$$

151 Here dN/dt is the event rate of a certain process and σ is its cross section. This rate is
 152 directly proportional to the frequency f , the number of bunches n and the number of
 153 particles in the two bunches N_1, N_2 , and inversely proportional to the beam cross-section
 154 A . The instantaneous luminosity is measured by dedicated subdetectors that are described
 155 in Section 2.3.

Integrating over the accelerator active time (a “fill”, when stable beams are kept colliding) gives the *integrated luminosity*, relating the total number of produced events N_{tot} to the cross-section:

$$\int \mathcal{L} dt = \frac{N_{tot}}{\sigma}. \quad (2.2)$$

156 In 2010 ATLAS collected about 45 pb^{-1} of p-p collision data at $\sqrt{s}=7 \text{ TeV}$, and in 2011
 157 reached about 5 fb^{-1} of the same data. In 2012, with $\sqrt{s}=8 \text{ TeV}$ collisions, LHC reached

Parameter	designed	2010	2011	2012
Beam energy (TeV/c)	7	3.5	3.5	4
Beta function β^* (m)	0.55	2.0/3.5	1.5/1.0	0.6
Max. No. bunches/beam	2808	368	1380	1380
Max. No. protons/bunch	1.15×10^{11}	1.2×10^{11}	1.45×10^{11}	1.7×10^{11}
Bunch spacing (ns)	25	150	75/50	50
Peak luminosity ($\text{cm}^{-2}\text{s}^{-1}$)	1×10^{34}	2.1×10^{32}	3.7×10^{33}	7.7×10^{33}
Emittance ε_n (μrad)	3.75	2.0	2.4	2.5
Max. $\langle \mu \rangle$	19	4	17	37

Table 2.1: Overview of some parameters for the LHC performance comparing the design values with their time evolution during the first long run operation in 2010-2013 [11].

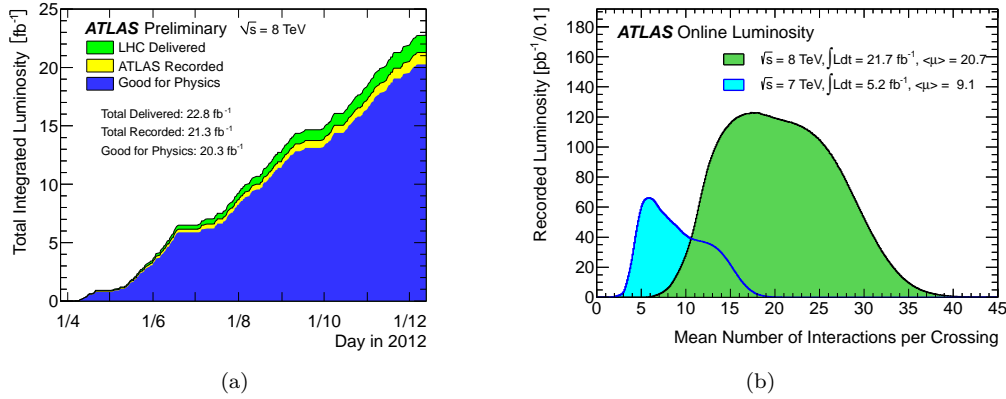


Figure 2.3: (a) Total integrated luminosity versus time delivered by the LHC to ATLAS (in green), recorded by the experiment (in yellow) and selected as “good data” for analysis (in blue) for p-p collisions at $\sqrt{s}=8 \text{ TeV}$. (b) Mean number of interactions per beam crossing during 2011 and 2012 LHC runs, where $\mu = \mathcal{L} \times \sigma_{\text{inelastic}}/f$ depends on the instantaneous luminosity \mathcal{L} , the p-p inelastic cross section $\sigma_{\text{inelastic}}$ and the revolution frequency f . [12]

158 a peak luminosity of $7.7 \times 10^{33} \text{ cm}^{-2}\text{s}^{-1}$ which is more than half the design luminosity, as
 159 shown in Table 2.1 together with other parameters relevant for the accelerator performance.
 160 Over 2012, the last year of data taking before the long shutdown³, ATLAS collected about
 161 20 fb^{-1} of p-p collision data at $\sqrt{s}=8 \text{ TeV}$. Figure 2.3(a) shows the delivered luminosity from
 162 the start of stable beams until beam dump and the luminosity recorded by ATLAS during
 163 stable beam conditions, the difference with respect to the delivered luminosity being due to
 164 Data Acquisition (DAQ) inefficiencies. Of the recorded luminosity, only a part is usable for
 165 analysis, and is what is called “good data”, i.e. the data that satisfy Data Quality (DQ)
 166 requirements assessed after reprocessing (see Section 2.5).

167 In order to increase the luminosity LHC operates with a high number of protons per
 168 bunch as well as a high number of bunches per beam and reduces the inter-bunch latency

³LHC terminated the p-p program at the end of 2012, operated proton-heavy ion collisions for two months at the beginning of 2013 and then stopped for what is called the first long shutdown. During this two-years time the accelerator and the experiments as well will undergo substantial maintenance and upgrade works, in order to be re-operated in 2015 with higher performance at a higher center of mass energy for particle collisions.

time. This overall defines a set of challenges that physics analysis will face associated to the high luminosity. Even at the detector design stage, the high frequency of collision environment foreseen influenced the choice of radiation resistance material for the experiment sub-systems. Concerning directly the physics instead, the main problematic is *pile-up*.

Pile-up events are distinguished between *in-time* and *out-of-time* pile-up. The first ones come from the multiple inelastic scatterings of protons in the same bunch, as if we consider a cross-section of 80 mb at the nominal luminosity of $10^{34} \text{ cm}^{-2}\text{s}^{-1}$ the number of events per second will be something like a billion. This translate, at a collision frequency of one crossing every 25 ns, to about 20 interactions per crossing that will be detected simultaneously. A useful observable to estimate in-time pile-up is the number of reconstructed primary vertices (see Section 4.2) N_{PV} . In addition, on the other hand, the inter-bunch time interval is so short that the electronics reading the detector might not keep up with the frequency of collisions, leading to the cumulation of events that happened in different beam crossings. This is the effect we refer to as out-of-time pile-up, and a good estimator for it is the average number of p-p interactions per bunch crossing at the time of the event, $\langle \mu \rangle$, which recalling Equation 2.1 is defined as:

$$\langle \mu \rangle = \frac{LA}{nf}, \quad (2.3)$$

with L being the average instantaneous luminosity over a time period $\Delta t \gg 600$ ns. The maximum values reached by the variable $\langle \mu \rangle$ during the three years of data taking are reported in Table 2.1.

Finally, ATLAS makes use of a three-level trigger system (described in Section 2.4) to identify and record only the events of interest, while the pile-up issues are dealt with at the analysis reconstruction level.

2.2 The ATLAS detector

ATLAS (A Toroidal LHC ApparatuS) [1] is a general purpose experiment aimed at exploring a vast range of physics scenarios and designed to measure the particles produced in p-p collisions at the LHC at unprecedented energies and instantaneous luminosities. It is the biggest detector of its kind ever built (it's 46 m long and 25 m high) is characterized by a full coverage of the space around the p-p interaction point and complete containment of the particles produced in the collision. Different subsystems are layered concentrically one after the other, each of them pursuing a specific task. Right around the interaction point (IP) where the LHC makes protons collide there is the Vertex Detector, reconstructing charged particles trajectories that are bent by the first solenoid magnet surrounding the Vertex Detector. Particles going through it then encounter the two calorimeter systems, the Electromagnetic and the Hadronic one. Muons are the only particles that will pass the calorimeters material (beyond neutrinos) and a dedicated Muon Spectrometer is the last piece of detector, embedded in a huge toroidal magnet. The detector complex is presented as a schematic in Figure 2.4, and a drawing of particle detection in the various subdetector systems is shown in Figure 2.5.

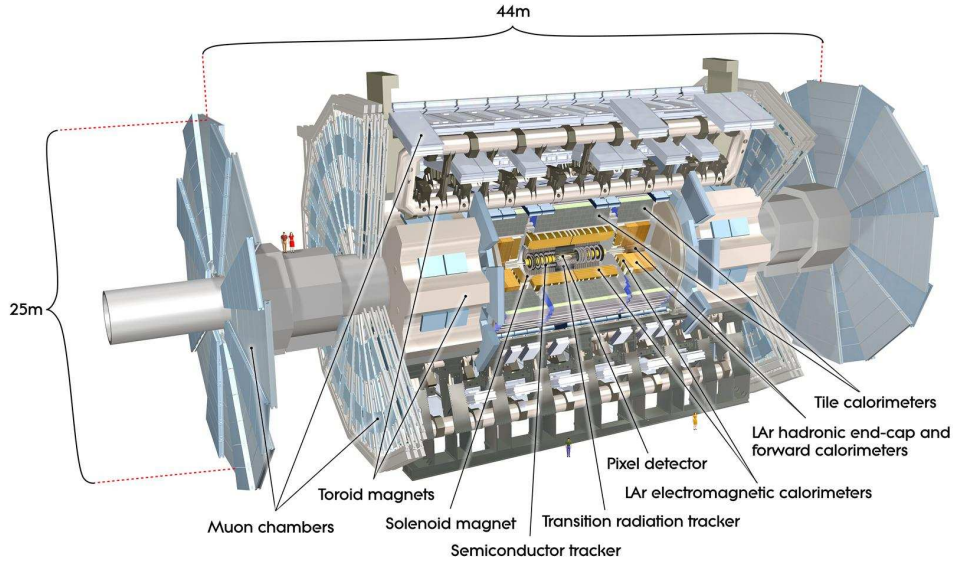


Figure 2.4: Schematic drawing of the ATLAS experiment. The detector subsystem are indicated as well as the total dimensions.

2.2.1 Coordinate system

Protons from the two circulating beams are made to collide in the center of the ATLAS detector, in the region that takes the name of Interaction Point (IP). The IP is taken as the origin of a three dimensional XYZ right-handed coordinate system. The Z axis is tangent to the trajectory of the beams while the XY plane is perpendicular to it and defines a symmetry plane for the detector, dividing it into the *A* and *C* sectors, respectively in the positive and negative Z semi-axes. Figure 2.6(a) shows a schematic of the coordinate system.

In terms of polar coordinates, the Z axis is again along the beam axis and in the transverse plane the *R* and ϕ coordinates are defined with ϕ ranging between $-\pi$ and $+\pi$ with respect to the X axis. In terms of spherical coordinates (see Figure 2.6(b)), the radial vector *R* originates from the IP, the azimuth ϕ is the same as the polar angle ϕ , and the polar angle θ is measured with respect to the Z axis and ranges between 0 and π .

Since the interaction initial energy is unknown, being dependent on the parton distribution functions for the proton energy, it is useful to define the transverse component of variables of interest⁴ like the energy and the momentum, being taken as the projection on the XY plane:

$$E_T = E \sin \theta, \quad p_T = p \sin \theta. \quad (2.4)$$

Another common variable used at hadron colliders to describe the polar distribution and

⁴These quantities transverse initial value will be, indeed, zero, as the protons are accelerated along the Z axis.

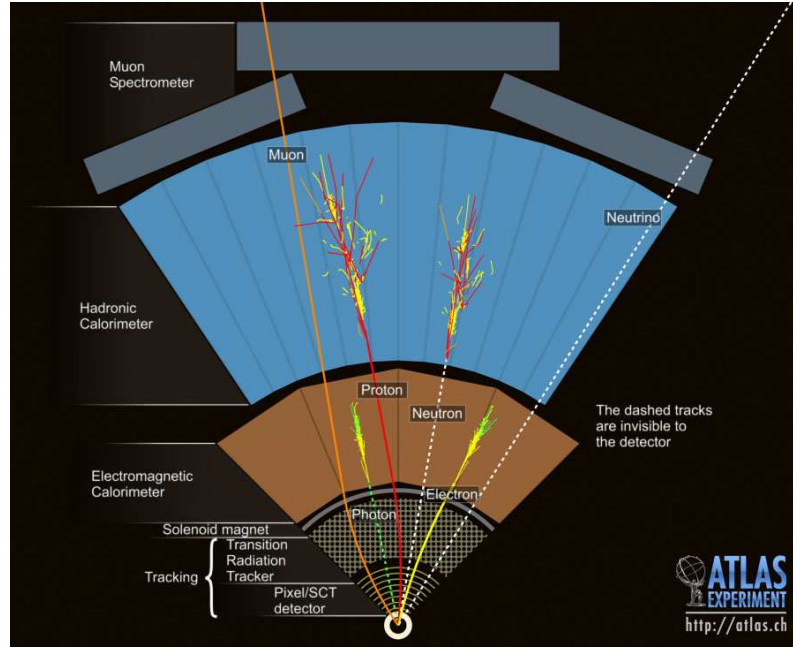


Figure 2.5: Drawing of the detection of particles going from the interaction point through the whole detector.

preferred to the simple polar angle θ is the pseudorapidity η :

$$\eta \equiv -\ln \left(\tan \frac{\theta}{2} \right); \quad (2.5)$$

which, for relativistic regimes, is equal to the rapidity y :

$$y \equiv \frac{1}{2} \ln \left(\frac{E + p_z}{E - p_z} \right); \quad (2.6)$$

and Δy and $\Delta \eta$ are Lorentz invariant. The pseudorapidity is preferred to the rapidity as it does not require knowing the particle mass but only its polar position. The distance between two particles is often referred to in terms of ΔR :

$$\Delta R = \sqrt{(\Delta \eta)^2 + (\Delta \phi)^2}. \quad (2.7)$$

Figure 2.6(b) shows how different pseudorapidity regions are named. Particles along the Z axis have a pseudorapidity $|\eta| = \infty$, particles along the Y axis have a pseudorapidity $|\eta| = 0$. ATLAS has an excellent hermeticity and is able to cover pseudorapidity regions up to $|\eta| = 4.9$. Typically, physics analysis consider objects in the pseudorapidity region $|\eta| < 2.5$. For a quick visualization of the correspondence in terms of polar angle distribution, some pseudorapidity values are reported in Table 2.2.

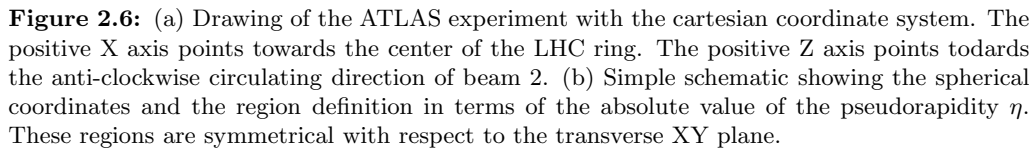


Table 2.2: Pseudorapidity vs polar angle values.

ATLAS is provided with four superconducting magnets that allow the measurement of charged particles momenta by curving their trajectory.

Paired to the muon spectrometer, the superconducting air-core toroid magnet (Figure 2.7) has an open structure with eight superconducting toroidal coils in the barrel part (each 25.3 m long, located at the outer diameter of 20.1 m) and two end-cap systems made of eight coils. The field strength varies strongly with ϕ : in the barrel region ($|\eta| < 1.4$) is 1.5-5.5 Tesla-m; in the end-caps ($1.6 < |\eta| < 2.7$) 1-7.5 is Tesla-m. Such configuration of the magnets gives a field orthogonal to the muons trajectory.

The Inner Detector (ID) is the subsystem closest to the IP and tracking charged particles arising from collisions allows for the measurement of their momentum and vertex reconstruction with excellent resolution. At the design choices level, radiation resistance had to be taken into account, as well as reducing the amount of material to be placed in front of

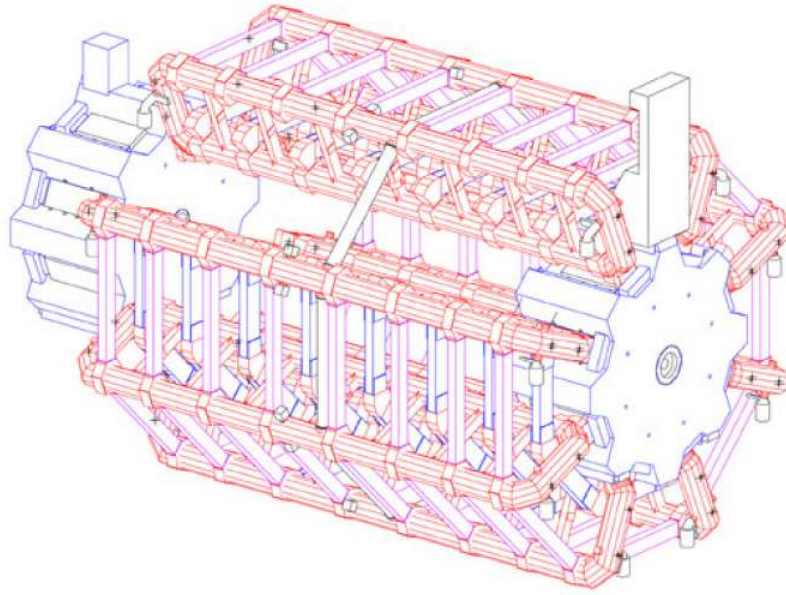


Figure 2.7: Toroidal magnet system.

the calorimeters to avoid spoiling the energy measurement. This quantity varies between 0.5 and $2.5 X_0$ depending on the pseudorapidity region, most of it coming from supporting equipment. This material is responsible for photon conversions and electron bremsstrahlung.

The ID is surrounded by the central solenoid magnet (Section 2.2.2) and is composed by three subsystems, from the closest to the furthest from the IP: the pixel detector, the SemiConductor Tracker (SCT) and the Transition Radiation Tracker (TRT).

Pixel detector

The first subsystem covers the region $|\eta| < 2.5$ and is composed by three cylindrical layers in the barrel region, each of them distant from the beam by 50.5 mm, 88.5 mm and 122.5 mm respectively, and by three concentric discs in the end-cap region, each of them distant from the beam by 49.5 mm, 58.0 mm and 65.0 mm respectively. Each silicon pixel has a size of $50 \times 400 \mu\text{m}^2$ and is $250 \mu\text{m}$ thick, with in total ~ 80.4 million readout channels to achieve a very fine granularity. The precision is of $10 \mu\text{m}$ in $R\phi$ and $115 \mu\text{m}$ in Z and R in the barrel and end-cap region respectively.

The very first layer is called B -layer as, thanks to its position really close to the IP, allows for the reconstruction of secondary vertices associated with the production of short lived particles such as B -hadrons. This information is very useful to identify jets originating from the fragmentation of b quarks.

Semiconductor tracker

After the three layers of pixel detectors, come four layers of silicon strip detectors. The SemiConductor Tracker (SCT) also covers the region $|\eta| < 2.5$ with a barrel and end-cap

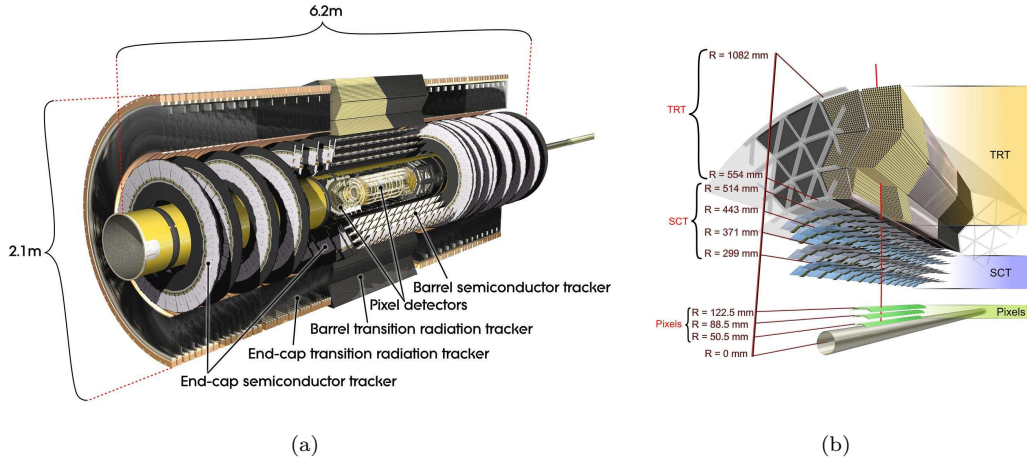


Figure 2.8: (a) Schematic of the ID system. (b) Detailed schematic of the barrel section of the ID showing the three subsystems and reporting the distance to the center of the beam pipe.

design similar to the pixel detector one, being composed by eight silicon strips (two per layer) 128 mm long and 80 μm large. It makes use of ~ 6.3 millions readout channels and the resolution achieved is of 17 μm in $R\phi$ and 580 μm in Z (R) in the barrel (end-cap) region.

By allowing for four redundant position measurements⁵, the SCT contributes mainly to the momentum reconstruction.

Transition Radiation Tracker

In order to reduce the amount of material in front of the calorimeters, and to reduce the construction costs as well, in the third subsystem the semiconductor technology has been substituted with straw detectors. The Transition Radiation Tracker (TRT) consists of thin proportional chambers made of straw polyimide drift tubes, 4 mm in diameter. The drift tubes are filled with a gas mixture composed of: 70% Xenon, 27% Carbon Dioxide, 3% Oxygen. The anode collecting the electrons from the ionized gas at the passage of the charged particle is made of tungsten covered in gold.

In the barrel region the tubes are 144 cm long and placed parallel to the beam axis, while in the end-cap region they are 37 cm long and positioned radially in wheels, with layers of radiator foils alternated to layers of straws. The resolution achieved is of 130 μm in $R\phi$ and $Z\phi$ in the two regions respectively. The covered pseudorapidity region is of $|\eta| < 2.0$ and the readout is composed by ~ 351000 channels.

About 36 measurements per track are taken, and since each channel provides two independent thresholds per hit, it is possible to discriminate between electrons and pions, since the former will more likely reach the high threshold.

In the end, the combination of the three ID subsystems gives very precise $R\phi$ and Z measurements, as well as good track pattern recognition. The resolution on the transverse

⁵One of the coupled layers is rotated of 40mrad with respect to the other, which is parallel to the axis, giving a small stereo angle for a redundancy in the ϕ coordinate measurement.

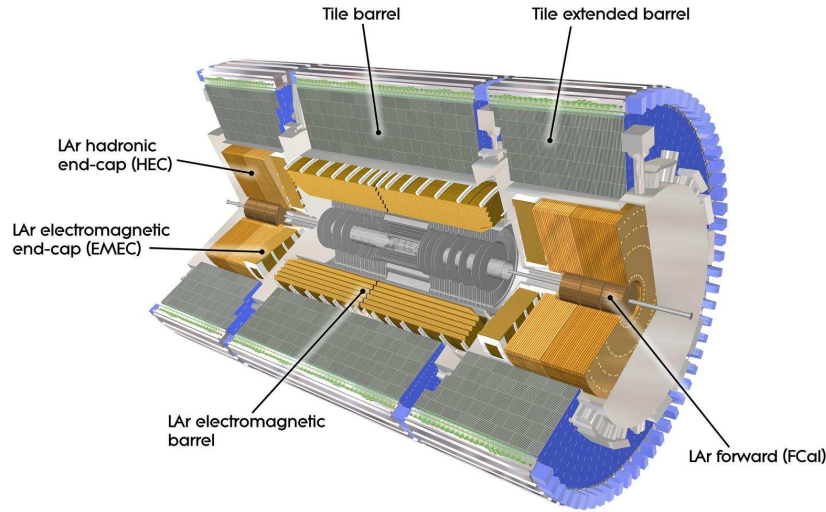


Figure 2.9: Schematic of the calorimeter complex of the ATLAS detector.

momentum, measured with cosmic muon calibration runs [13], is:

$$\frac{\sigma_{p_T}}{p_T} = P_1 \oplus P_2 \times p_T, \quad (2.8)$$

where $P_1 = 1.6 \pm 0.1\%$ and $P_2 = (53 \pm 2) \times 10^{-5} \text{ GeV}^{-1}$. This means a resolution of $\sim 1.6\%$ for tracks with $p_T \sim 1 \text{ GeV}$ and $\sim 50\%$ for tracks with $p_T \sim 1 \text{ TeV}$.

2.2.4 Calorimeters

Particles leaving the ID and surviving the crossing of the central solenoid magnet will face the calorimeter system, depicted in Figure 2.9. The full system is characterized by a coverage in pseudorapidity up to $|\eta| < 5$ and an almost full coverage in ϕ . With its $22 X_0$ and $24 X_0$ radiation lengths of material in the barrel and end-cap regions respectively it is also able to stop most of the non-muon particles from the interaction. Besides particles energy measurement, the calorimeters provide particle identification information, discriminating electrons, photons and jets, and the determination of the missing transverse energy.

Different technologies are used in the barrel, end-cap and forward regions for both the electromagnetic and the hadronic calorimeters. All of them are sampling calorimeters, with a dense medium acting as absorber to stop particles and start showers, and an active material to detect the signal from ionization. For the electromagnetic calorimeters and the forward hadronic calorimeter liquid argon is used as active medium, while the barrel and extended-barrel hadronic calorimeter uses scintillating tiles. The liquid argon is cooled at a temperature of about 88 K, with the use of two sets of cryostats: the barrel electromagnetic calorimeter shares the cryostat with the central solenoid; the end-cap and forward electromagnetic calorimeter and the hadronic end-cap calorimeter share a cryostat in the forward region.

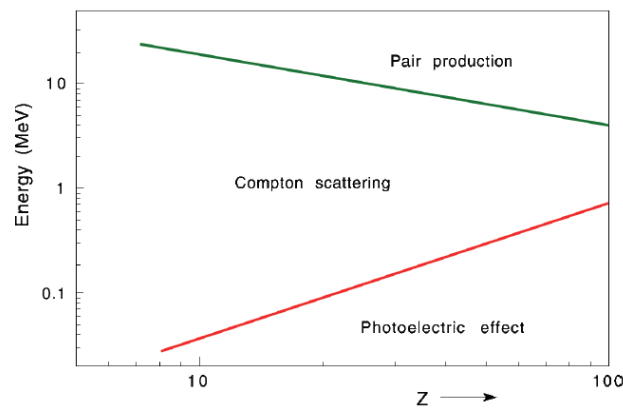


Figure 2.10: Domains in term of photon energy and Z number of the absorber material in which photoelectric effect, Compton scattering and pair production are the favorite processes for energy loss [14].

Particles interact both with the passive and active material, but only the energy released in the active samples will be detected. The processes involved in the shower formation are several and mainly electromagnetic. Photons in matter can undergo the photoelectric effect, Compton scattering and $\gamma \rightarrow e^+e^-$ pair formation. The general contribution of these processes depends both on the photon energy and on the atomic number Z of the material, and is shown in Figure 2.10. Electrons and positrons can ionize atoms and molecules, produce bremsstrahlung $e^\pm \rightarrow e^\pm + \gamma$ and emit Cerenkov radiation. Unless the calorimeter has been specifically designed for it, Cerenkov radiation does not contribute much, while ionization is the main process for energies up to ~ 100 MeV, where bremsstrahlung starts to dominate.

In general, these cascade of events continues until a certain threshold is reached, and the final number of particles produced is proportional to the energy of the first particle originating the shower.

Also hadrons interact with matter, either ionizing it (if charged) or by nuclear interactions. The problem of the latter process is that this energy release is often not directly detectable, like in nuclear breakups and excitations, and is therefore called “invisible energy”. Secondary hadrons will be produced, forming the hadronic part of the shower, but sooner or later something like $\pi^0 \rightarrow \gamma\gamma$ will happen and the shower will develop electromagnetically further on.

The average fraction of electromagnetic and hadronic shower components is a characteristic of the sampling calorimeter and depends on the choice of the passive and active material and on the design. Calorimeters are said to be *non-compensating* if, like the ATLAS calorimeters, the detection of hadronic showers is less efficient than the one of electromagnetic showers. Calorimeters with a similar response for the two components are called *compensating*, while calorimeters more efficient when revealing hadronic showers are *over-compensating*.

The performance for the energy resolution is parametrized by the following formula:

$$\frac{\sigma_E}{E} = \frac{S}{\sqrt{E}} \oplus \frac{N}{E} \oplus C, \quad (2.9)$$

where the terms of the sum correspond, respectively, to a “stochastic” term related to how shower develops in the sampling calorimeter; to a “noise” term including the contribution from electronic noise and pile-up energy fluctuation; to a systematic term that depends on calibration, shower containment, inactive material and on the linearity of the response as well.

The goal energy resolution for the liquid argon calorimeters is [15]:

$$\frac{\sigma_E}{E} = \frac{10\%}{\sqrt{E}} \oplus \frac{170 \text{ MeV}}{E} \oplus 0.7\%, \quad (2.10)$$

while for the hadronic barrel calorimeter is [16]:

$$\frac{\sigma_E}{E} = \frac{50\%}{\sqrt{E}} \oplus 5\%. \quad (2.11)$$

Test-beam runs to measure the response of the two calorimeters to electrons and single pions respectively have shown results comparable to the goal resolutions.

Electromagnetic calorimeter

The electromagnetic calorimeter, also called LAr calorimeter (from Liquid Argon, the active material), can measure electrons and photons energies in the range from 50 MeV to 3 TeV. In the barrel region it is referred to as EMB (ElectroMagnetic Barrel), is divided into two identical semi-barrels EMBA and EMBC separated at Z=0 by a 6 mm gap and covers the pseudorapidity region $|\eta| < 1.475$. Two end-cap detectors (EMEC, ElectroMagnetic End-Cap), divided into two coaxial wheels, cover the pseudorapidity regions $1.375 < |\eta| < 3.2$. A pre-sampler, extended over $|\eta| < 1.8$, stands in front of the EMB and allows for the measurement of the energy the particles lost before reaching the EMB i.e. crossing the material of the ID, the central solenoid and the cryostat.

Three longitudinal samples in the EMB are designed for different tasks. The first sample, $4.3X_0$ long, is finely segmented in η to precisely measure the direction in pseudorapidity of the particles with thin readout strips of $\Delta\eta \times \Delta\phi = 0.0031 \times 0.098$. This helps for photon/ π^0 discrimination and as well for separate close-by γ s from π^0 decay. The second sample, $16X_0$ long, contains the bulk of electrons and photons energy deposit. It is divided in towers with dimension $\Delta\eta \times \Delta\phi = 0.025 \times 0.0245$ and provides the position measurement of the cluster. The 95% of the energy of the shower is deposited in a matrix of 3×7 towers $\Delta\eta \times \Delta\phi$. The third sample, $2X_0$ long, is coarsely segmentes and collects the last bit of the longitudinal development of the electromagnetic showers. Towers in this region have a dimension of $\Delta\eta \times \Delta\phi = 0.05 \times 0.0245$.

Also the EMEC is divided in three longitudinal samples (two in the region $1.375 < |\eta| < 1.5$), and besides the lead, also the thickness of the liquid argon layers are varied in the radial direction.

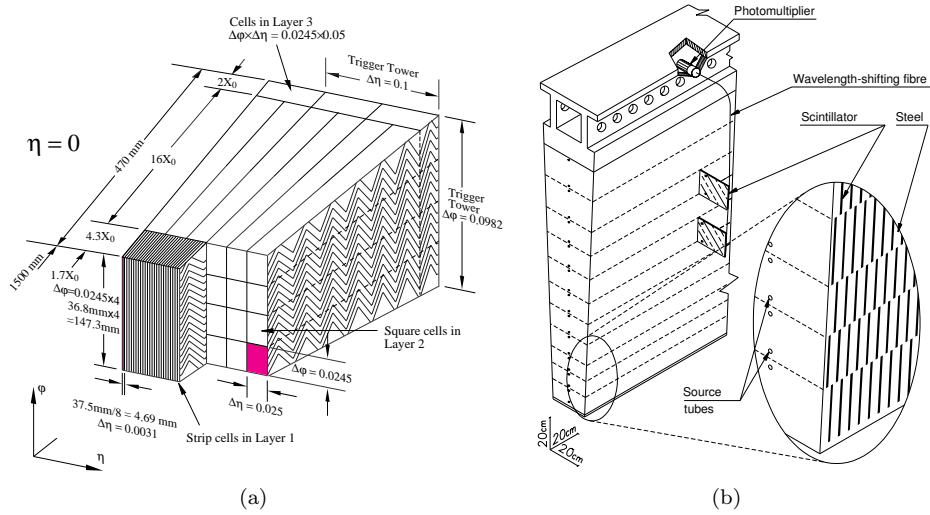


Figure 2.11: (a) Schematic drawing of a module of the Electromagnetic barrel calorimeter. (b) Schematic drawing of a module of the Hadronic barrel calorimeter.

The absorbing material is lead shaped into an accordion geometry to achieve full symmetry in ϕ , as shown in the drawing of Figure 2.11(a). Signal from the ionization produced in the liquid argon is collected by an electrode in the middle of the active material region, fixed into a honeycomb structure.

The thickness of the absorber layers depend on the pseudorapidity in order to make particles entering the system with different incident angles cross the same amount of material.

Hadronic calorimeters

Hadronic showers have typically a much longer shape than electromagnetic ones, and need therefore in general more interaction lengths of material to be fully contained. Hadronic calorimeters are therefore designed to completely absorb high-energy hadrons, which will deposit only some (small) part of their energy in the electromagnetic calorimeter.

Hadronic barrel calorimeter

The hadronic calorimeter in the barrel and extended barrel region, going up to $|\eta| < 1.7$, is made of scintillating tiles as active material with lead as absorber and is commonly referred to with the name of TileCal. The light in the ultraviolet range that is generated in the tiles is collected through wavelength shifting optical fibre (Figure 2.11(b)).

TileCal sits just after the electromagnetic calorimeter and measures the energy and position of jets and isolated hadrons. It is divided in depth in three layers with varying length (1.4, 4.1, 1.8 hadronic interaction lengths λ in the barrel and 1.5, 2.6, 3.3 λ in the extended barrel) and segmentation ($\Delta\eta \times \Delta\phi = 0.1 \times 0.1$ in the first two layers, $\Delta\eta \times \Delta\phi = 0.2 \times 0.1$ in the third), and in 64 slices in ϕ , each of $\Delta\phi \sim 0.1$.

The readout channels are grouped into cells that form a pseudo-projective geometry in η .

Hadronic end-cap calorimeter

The Hadronic End-Cap calorimeters (HEC) use copper as passive material and liquid argon as active material, chosen for its radiation hardness in a region ($1.5 < |\eta| < 3.2$) exposed to a significant amount of particle flux. Each HEC is composed by two independent wheels with granularity varying with η : in $1.5 < |\eta| < 2.5$ $\Delta\eta \times \Delta\phi$ is 0.1×0.1 in the first two longitudinal layers, 0.2×0.1 in the last one; in $2.5 < |\eta| < 3.2$ $1.5 < |\eta| < 2.5$ $\Delta\eta \times \Delta\phi = 0.2 \times 0.2$ in all the three samples.

The HECs collect the energy from particles that are not completely contained in the EMECs and in particular are used to reconstruct jets and the missing transverse energy.

Forward calorimeter

The Forward Calorimeter (FCal) cover the very forward region of pseudorapidity $3.1 < |\eta| < 4.9$ making the calorimeter system achieve its good hermeticity and minimize the energy losses. It has an electromagnetic part that uses copper as absorber and two hadronic compartments with tungsten as passive material.

2.2.5 Muon spectrometer

The most external detector system is the muon spectrometer, a combination of toroidal superconducting magnets (Section 2.2.2) and precision chambers providing a measurement of the momentum of muons in $|\eta| < 2.7$ in addition to the measurement from the ID. It is also equipped with an independent trigger system used for the first event triggering stage (see Section 2.4.1) active in the pseudorapidity region $|\eta| < 2.4$.

Four sub-detectors compose the muon system: Monitored Drift-Tube (MDT) chambers, Cathode Strips Chambers (CSC), Resistive Plate Chambers (RPC) and Thin Gap Chambers (TGC). The layout changes in the barrel and end-cap regions, and is schematically shown in Figure 2.12(b): in the barrel region, chambers are arranged in three cylindrical layers around the beam axis, one layer being inside the magnet; in the end-caps these three layers are placed perpendicular to the beam axis.

Detection chambers

MDTs and CSCs are used to detect muons in the pseudorapidity regions $|\eta| < 2.0$ and $2.0 < |\eta| < 2.7$ respectively. MDTs are proportional chambers constituted by pressurised drift tubes made of aluminium with a diameter of 30 mm and lenght varying from 0.9 m to 6.2 m. The gas mixture in them is 93% argon and 7% carbon dioxide, the anode is a $50 \mu\text{m}$ tungsten-rhenium wire producing a radial electric field. Each chamber is composed by a group of six or eight tubes placed transverse to the beam axis. This number of tubes allows for a very good track reconstruction and high reduction of the fake tracks from random associations of background hits, providing a resolution on position of $80 \mu\text{m}$.

The CSCs are used at higher η to better cope with the higher particle flux. They are arranged in a system of two disks with eight chambers each. Each chamber contains four multiwire proportional chambers (the CSCs) with wires oriented in the radial direction, spaced by 2.5 mm and in the same gas mixture of argon and carbon dioxide as the MDTs.

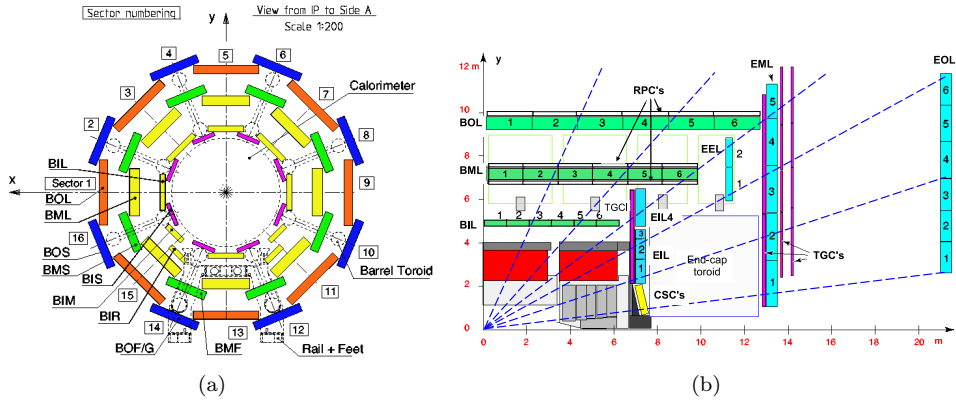


Figure 2.12: (a) Cross section of the barrel muon system. (b) Lateral section of the muon system. Barrel MDTs are shown in green, end-caps MDTs in light blue, CSC in yellow, TGCs in magenta, RPCs in white.

The cathode strips are oriented one perpendicularly to the anode wires (and gives the precision coordinate) and the other parallel to the wires (and gives the transverse coordinate). The resolution provided by the interpolation between the charges induced on neighbouring cathode strips ranges between 50 and 70 μm .

Trigger chambers

For trigger purposes detectors with faster response than drift tubes are needed⁶. MDTs and CSCs are then coupled with special layers of trigger chambers: in the barrel region, the MDT's second layer is covered on both sides by RPCs, while MDT's third layer is covered by a RPC alternatively on the inner and outer side; in the endcaps, TGCs cover the inner side of MDT's first and third layers.

A RPC is a detector with a gas-gap between two resistive bakelite plates separated by 2 mm and containing a gas mixture of $\text{C}_2\text{H}_2\text{F}_4$ (94.7%), $\text{Iso-C}_4\text{H}_{10}$ (5%) and SF_6 (0.3%). RPCs measure six points per coordinate for each particle, quickly collecting the avalanches with two orthogonal sets of pick-up strips that provides a position resolution of 1 cm in each plane and 1 ns time resolution, allowing for individual bunch crossing discrimination. Also RPCs provide the ϕ coordinate for the tracks in the final analysis, since MDTs only give the η coordinate.

TGCs are similar to CSCs, have 1.8 mm wire-to-wire separation and 1.4 mm wire-to-cathode separation. They use a highly quenching gas mixture of CO_2 55% and $\text{n-C}_5\text{H}_{12}$ 45% and provide a spatial resolution of about 1 mm and a time resolution of 5 ns.

2.3 Forward sub-detectors

ATLAS is equipped with some detectors in the forward regions to perform additional measurements or monitoring studies. In particular, the Minimum Bias Trigger Scintillators

⁶Drift-time in tubes with a diameter of $\mathcal{O} \sim 10$ mm can be of ~ 500 ns, too long with respect to the 25 ns spacing of the bunch crossings.

Figure 2.13: Schematic of a section of TileCal barrel and extended barrel modules, with the cells division. The parts labelled with “E” are the MBTS.

(MBTS), that are somehow embedded in the structure of TileCal extended barrel modules (see Figure 2.13) and share with it the readout electronics, as they are also read by wavelength-shifting fibers. The MBTS consist of 32 scintillator paddles assembled in two disks covering the pseudorapidity region $2.09 < |\eta| < 3.84$ and are used for trigger purposes to detect minimum bias activity during the first runs of the LHC.

MBTS are also used for relative luminosity measurements, but there are two detectors specifically built to determine the luminosity delivered to ATLAS: LUCID and ALFA. LUCID (Luminosity measurements using Cerenkov Integrating Detector) is made of 32 tubes surrounding the beam pipe 17 m far from the interaction point on both sides of ATLAS and measures the luminosity bunch by bunch. ALFA (Absolute Luminosity For ATLAS) is only activated during special runs, and consists of 8 scintillating fibers detectors placed at 240 m from the interaction point inside roman pots, above and below the beam pipe.

Another luminosity monitorer is the Zero-Degree Calorimeter, whose main purpose is to determine the centrality of heavy-ion collisions. Placed at 140 m from the interaction point on both sides of the beam axis, is made of quartz rods alternated with tungsten plates.

Finally, the Beam Condition Monitor (BCM) is made of two sets of diamond sensors located 184 cm close to the interaction point along the beam and 5.5 cm close along R . Its task is to detect beam losses, potentially harmful for ATLAS, and in that case to alert LHC in order to stop the accelerator.

2.4 Trigger system

It was already introduced at the beginning of this Chapter the issue faced by LHC experiments of dealing with a huge amounts of events at very high frequencies. We remind that considering the nominal LHC luminosity of $10^{34} \text{ cm}^{-2} \text{ s}^{-1}$ a rate of interactions of 40 MHz is expected! This poses serious technical difficulties as the maximum frequency at which data can be recorded is limited to 200 Hz considering the limited capacity for storage.

ATLAS developed a trigger system able to reduce by a factor of 10^6 the amount of data to be kept by selecting only interesting physics events. The system is divided in three levels characterized by increasing sophistication and diminishing speed. At the very first indeed we will need a really quick and simple criterium to reject uninteresting events. The reduced information can then be processed with somehow slower logic by the other two High Level Triggers (HLT). A drawing of the system is shown in Figure 2.14.

Most of the trigger chains used for physics are un-scaled in the sense that all the events passing the selection are kept, but there are also pre-scaled trigger chains that contain either too many events or events considered not physically interesting. These trigger chains are used for checks or calibration rather than physics analysis, and the prescaling value P means that of all the events that would have passed the trigger, $1/P$ were accepted.

With the term “trigger chain” we refer to the sequence of selections defining a certain

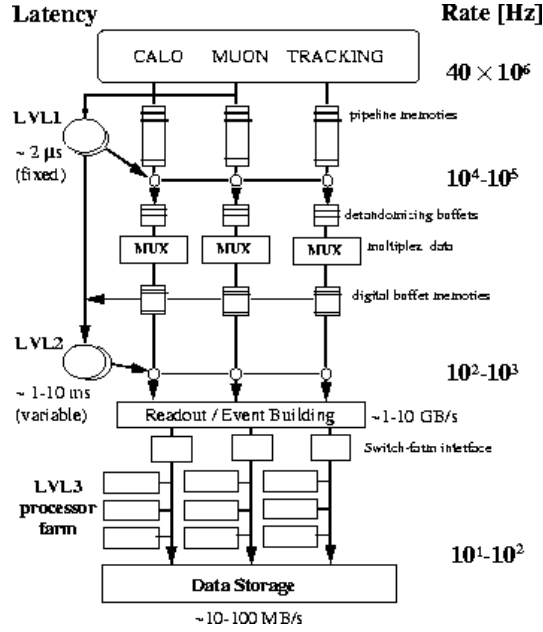


Figure 2.14: Schematic drawing of the three-level trigger system of ATLAS.

trigger object, with a naming convention like:

$$[\text{LEVEL}][\text{N}][\text{TYPE(S)}][\text{THRESHOLD}][\text{ISOLATION}][\text{QUALITY}],$$

where the components, from left to right, are: the trigger level used; the multiplicity of the type; the object candidate; the threshold applied to the transverse momentum or energy of the object candidate; the object isolation; the severity of the final algorithm requirements (this applies only to the Event Filter level).

Trigger chains define a *trigger menu*, where they are associated to their prescale value P , and which is chosen based on the physics program of the data taking period taking into account the LHC luminosity.

Defining the data taking period time unit as “Luminosity Block” (LB), typically a few minutes of data taking, information on beam conditions, detector performance and events passing any of the trigger chains of the trigger menu are stored to be then used in the analyses. All the LB occurring between the start and the end of a stable beam collision period compose a “run”. Runs are finally grouped in “Data Periods”, labelled with capital letters (“Period A”, “Period B”, *etc.*), when they pertain to the same general detector condition, machine configuration and trigger menu.

2.4.1 Level 1 trigger

The Level 1 trigger (L1) is completely based on the hardware of the detector, taking information from calorimeters, from the muon spectrometer trigger systems RPC and TGC (Section 2.2.5) and from the MBTS (Section 2.3) at 40 MHz (the frequency of the beam crossing) and reducing it to 75 kHz by choosing events with high transverse momentum or

high missing transverse energy.

Using dedicated fast front-end electronics (the typical decision time being less than $2\ \mu\text{s}$), calorimeter cells are analogically summed to build calorimetric towers which, if having an energy higher than a certain threshold, will activate a trigger chain.

These trigger chains will then be combined with the information from the muon spectrometer to form the so-called Region of Interest (RoI) that is passed to the next trigger level.

2.4.2 Level 2 trigger

Starting from the RoI, the Level 2 trigger (L2) will reduce the 75 kHz to 3.5 kHz of events with an average decision time of 40 ms. At this stage the information from the trackers is incorporated to the RoI to build candidate object (electrons, photons, muons) and better obtain its position and energy with simplified algorithms quick enough to respect the limit on the decision time.

2.4.3 Event filter

The last trigger, Level 3, is called Event Filter (EF) since at this point the physics objects are built using the same algorithms as the off-line reconstruction, with looser selections. With an execution time amounting to 4 s, the EF reduces the event rate to the goal value of 200 Hz. Events passing the EF are assigned to *streams* defined to separate the events into different datasets for different analysis interests, e.g. electron streams, muon streams, jet streams *etc.*

As an example, one of the trigger chains used in our analysis is `EF_mu24i_tight`: it selects events at the EF level with one muon with $p_T > 24\ \text{GeV}$ and some isolation requirement which passes the muon reconstruction algorithm cuts defined as “tight” (more on event reconstruction is reported in the dedicated Chapter 4).

2.5 Data Quality

The totality of p-p collisions recorded by ATLAS, which differs from the amount delivered by the LHC because of data-taking inefficiencies, is still not 100% usable by physics analyses. Indeed, every subdetector needs to perform some routine checks on the quality of the data they recorded in order to certify that its performance was conform to the expectations. So-called “Good Runs Lists” (GRL) are compiled stating for each LB what was “OK” and what not. The single analyses will then decide which GRL to use, based on their specific needs of the individual subsystems.

529 Monte Carlo simulation

530

531 In science, little should be left to chance. Still, randomness over a huge number of trials
 532 leads to insights of something we could consider as “real”. This is particularly useful when
 533 dealing with complex environments that can be described with a mathematical model in
 534 order to know what to expect from the actual data. Monte Carlo methods can describe
 535 hadron-hadron collisions, using pseudorandom numbers to simulate event-by-event fluctua-
 536 tions, and hence help us e.g. understanding the detector response and developing analysis
 537 strategies by predicting the sensitivity to the physics under study.

538 In this chapter, we will first go through a very brief overview of some concepts of the
 539 Quantum Chromodynamics theory useful to understand the evolution of a p-p collision event
 540 (Section 3.1). Thanks to perturbation theory we can predict hard scattering cross sections,
 541 which is what is done as the first step of the Monte Carlo simulation chain, described
 542 in Section 3.2.1. Despite the theoretical ability to compute fixed order calculations for
 543 hard scattering cross sections, we still lack the possibility to describe QCD at low energy
 544 and, hence, hadron final states formation. *Shower algorithms* can associate to an hard
 545 event an arbitrary number of partons to constitute a final state with quarks and gluons
 546 (see Section 3.2.2). The *hadronization* of this yet unphysical final state is performed by
 547 means of phenomenological models of hadron formation, introduced in Section 3.2.3). The
 548 last ingredient for a complete picture is the treatment of the remnants from the incoming
 549 protons from which the hard interacting partons came from. For this we rely on the so-called
 550 “underlying event model”, discussed in Section 3.2.4.

551 Finally, the products from the generated event are passed through a simulation of the
 552 ATLAS systems and digitized to give an output identical to the real detector one (Sec-
 553 tion 3.4). At this point objects are reconstructed in the same way for Monte Carlo and real
 554 data, as discussed in Chapter 4.

555 3.1 Phenomenology of p-p collisions

556 Of the interactions making up the processes, for Monte Carlo simulating hadron colliders
 557 physics the most challenging part is related to the description of Quantum Chromodynamics

(QCD) phenomenology. Indeed, despite its theoretical framework being successful and verified, calculations are difficult and often need approximations.

3.1.1 Proton structure

The proton is a bound state of three *valence* quarks which carry each a fraction x of the proton momentum unpredicted theoretically and described by parton distribution functions (PDFs) $f_i(x)$. The probability for a parton i to carry a momentum fraction between x and $x + dx$ is $f_i(x)dx$ and the following condition holds:

$$\int_0^1 x \sum_i f_i(x) dx = 1. \quad (3.1)$$

PDFs are measured in deep inelastic scattering experiments and are universal, not depending on the particular process used. It is observed that the valence quarks only carry about half of the proton total momentum, the rest being carried by virtual gluons continuously exchanged by the quarks. These gluons in turn produce virtual $q\bar{q}$ pairs called *sea* quarks.

Various parametrizations are available and the most widely used come from the CTEQ and MRST/MSTW collaborations¹ The 2008 NLO 68 version of PDFs of valence quarks, gluon and sea quarks from the MSTW group are shown in Figure 3.1 as a function of the momentum fraction for two values of transferred momentum Q^2 at which the proton is probed.

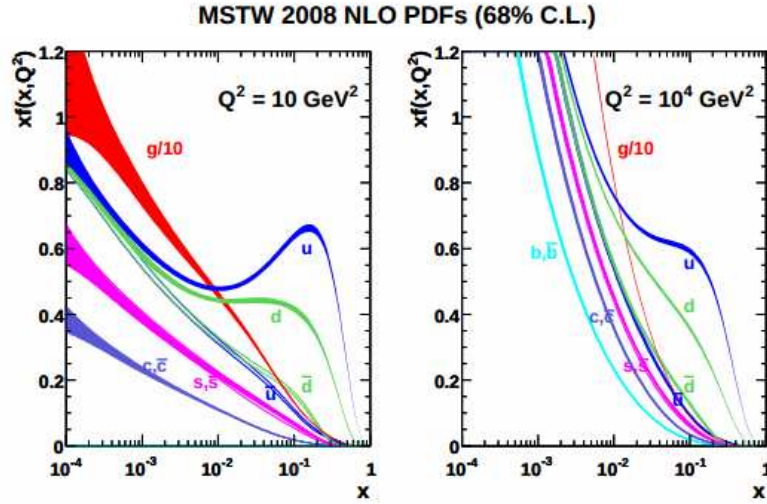


Figure 3.1: Proton PDF functions at transfer momentum $Q^2=10$ GeV ($Q^2=10000$ GeV) on the left (right) [17].

¹See for more information the Les Houches Accord PDFs (LHAPDF): <http://lhpdf.hepforge.org/> and the collaborations pages: <http://www.phys.psu.edu/cteq>, <http://mstwpdf.hepforge.org/>.

3.1.2 Factorization theorem

To treat infinities arising from divergent contributions in loop diagrams, an arbitrary renormalization scale μ_R is to be introduced. As a consequence from requiring that the physical observables be independent from the choice of μ_R , the strong coupling constant α_S does depend on the energy scale at which the coupling is observed and is, at the leading order:

$$\alpha_S(\mu^2) = \frac{\alpha_S(\mu_R^2)}{1 + (11 - \frac{2}{3}n_f) \frac{\alpha_S(\mu_R^2)}{2\pi} \ln \frac{\mu^2}{\mu_R^2}}, \quad (3.2)$$

with n_f being the number of quark flavors of the theory and μ the energy at which we observe the process.

This means that the coupling α_S decreases with increasing energy scale (small distances) as a consequence from the factor $11 - \frac{2}{3}n_f$ (the number 11 coming from the self interaction of gluons) being positive in the theory with $n_f = 6$, while it increases at lower energies (high distances). These two properties go under the name of *asymptotic freedom* and *confinement* respectively: at low α_S quarks and gluons interact very weakly with each other and it is possible to use perturbation theory and the parton model [18], which treats partons as free and non-interacting; when α_S is large instead, partons tend to bound together into colorless hadrons, predictions from perturbative calculations become less reliable and soft QCD interactions are typically modeled using tunings from experimental data.

The *factorization theorem* [19] allows us to separate the two components to compute the cross section as a product of probability functions with the short distance cross section $\hat{\sigma}_{ab}$ computable in perturbation theory (pQCD, from perturbative QCD) as a power expansion of the strong coupling constant $\alpha_S(\mu_R)$:

$$\begin{aligned} \sigma_{pp \rightarrow X} &= \sum_{a,b} \int_0^1 dx_a dx_b f_a(x_a, \mu_F) f_b(x_b, \mu_F) \hat{\sigma}_{ab}(x_a p_a, x_b p_b, \mu_R, \mu_F) \\ &= \sum_{a,b} \int_0^1 dx_a dx_b f_a(x_a, \mu_F) f_b(x_b, \mu_F) \times [\hat{\sigma}_0(\hat{s}) + \alpha_S(\mu_R^2) \hat{\sigma}_1(\hat{s}, \mu_F^2) + \dots]. \end{aligned} \quad (3.3)$$

Here, f_i ($i = a, b$) are the standard PDFs for partons $a, b = \{g, u, \bar{u}, d, \dots\}$ carrying fractions x_a, x_b of the proton longitudinal momentum, and $\sigma_{pp \rightarrow X}$ is the partonic scattering cross-section calculated in fixed-order perturbation theory. The μ_F coefficient is newly introduced *factorization scale*, μ_R is the renormalization scale for the QCD running coupling. Figure 3.2 shows a pictorial representation of the generic p-p process.

Equation 3.3 refers to a sum of final state and is, therefore, inclusive. The choice for the renormalization and factorization scale values is usually to take them of the order of some typical hard scale entering the process like, e.g., the mass of the top quark for top-anti-top pair production. The cross section calculations are done in pQCD are in general either provided at Leading Order (LO) or at Next-to-LO (NLO). NLO calculations include corrections from virtual exchange or emission of a massless parton.

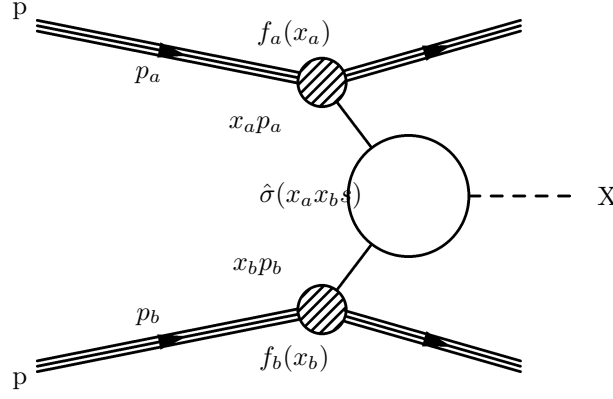


Figure 3.2: Diagram of a generic hard scattering process. The partons, extracted from the colliding p-p pair, carry a momentum fraction with respect to the proton energy described by a parton distribution function. The scattering of the partons is computed perturbatively and hence the kinematic properties of the final state object X are predicted.

3.2 Simulation of p-p collisions

The most interesting phenomena under study are scattering events with large momentum transfer or with production of massive particles, also called “hard scattering” events. Typical pQCD calculations can only provide an inclusive description of the process, while Monte Carlo programs give an exclusive picture of the event. A p-p collision event in Monte Carlo simulation is the combination of different sub-processes, illustrated in Figure 3.3: it comes with a large library of Standard Model and Beyond Standard Model cross section from which the hard scattering process is chosen; it has a showering algorithm to generate the dominant pQCD effects, adding the emission of colored partons to the hard process enhanced with collinear and soft singularities; it implements hadronization for the high energy partons of the final state; it describes the underlying event according to some phenomenological model; it includes libraries for the weak decay of unstable hadrons.

A set of drawings in Figure 3.4 shows the sequence of the evolution of Monte Carlo event simulation, starting from the plain hard scatter and adding step by step the other components.

3.2.1 Hard interaction

Recalling what discussed in Section 3.1.2 about the computation in pQCD of the hard scattering cross section of a typical LHC $pp \rightarrow X$ event, we can rewrite Equation 3.3 as:

$$\begin{aligned} \sigma_{pp \rightarrow X} &= \sum_{a,b} \int dx_a dx_b \int f_a(x_a, \mu_F) f_b(x_b, \mu_F) d\hat{\sigma}_{ab}(x_a p_a, x_b p_b, \mu_R, \mu_F) \\ &= \sum_{a,b} \int dx_a dx_b \int d\Phi_X f_a(x_a, \mu_F) f_b(x_b, \mu_F) \times \frac{1}{2x_a x_b s} |\mathcal{M}_{ab}|^2(\Phi_X, \mu_R, \mu_F), \end{aligned} \quad (3.4)$$

where we introduced the dependence on the final state phase space Φ_X , the parton flux $\frac{1}{2x_a x_b s}$ (with s being the center of mass energy squared) and the *matrix element* \mathcal{M}_{ab} ,

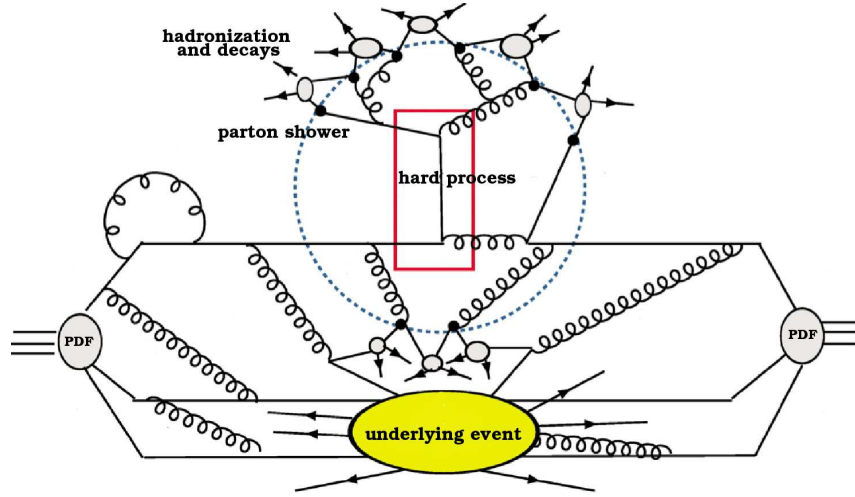


Figure 3.3: Drawing describing a hadron-hadron collision from the Monte Carlo point of view. Partons from the hadron share its energy according to the PDFs. The dotted circle separates pQCD events (hard scattering and initial and final state radiation) from non-perturbative effects (parton shower, hadronization, initial emissions included in the PDFs, and underlying event)[20].

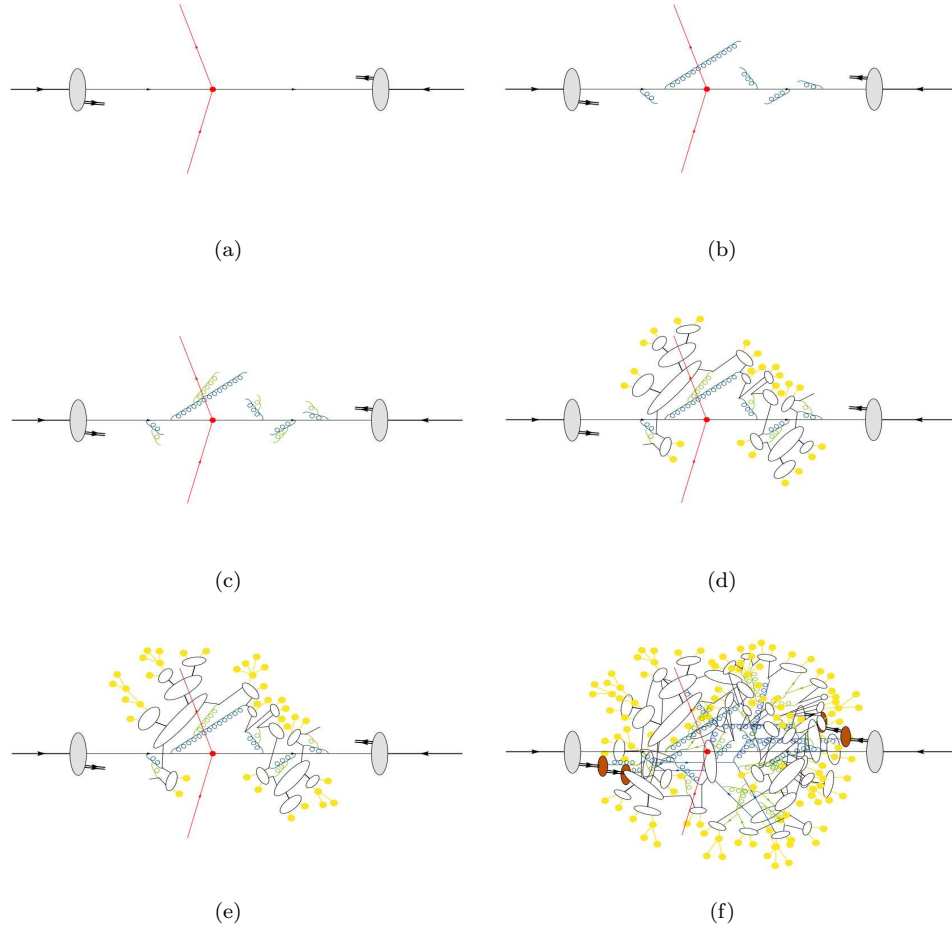


Figure 3.4: Set of frames of Monte Carlo event generation evolution: (a) hard scattering of two partons; (b) and (c) parton showering; (d) hadronization; (e) final particle decays; (f) underlying event simulation. Drawings from [21].

which is also written as a sum over Feynman diagrams:

$$\mathcal{M}_{ab} = \sum_i \mathcal{F}_{ab}^{(i)}. \quad (3.5)$$

3.2.2 Parton shower

Parton shower adds higher order corrections to the hard scatter using an approximation scheme, since real radiative corrections to any inclusive quantity (like the hard cross section as computed at fixed order in pQCD) are divergent. The dominant contributions below a cut-off parameter, associated to collinear parton splitting or soft gluon emission, are included iteratively ordered in sequence of, typically, smaller emission angles.

There are three possible processes for QCD emission: $q \rightarrow gq$, $g \rightarrow gg$ and $g \rightarrow q\bar{q}$. The cross section then factorizes into the product of the parent parton production cross section times a splitting factor. Considering e.g. the $q \rightarrow gq$ splitting from a tree level process with $n+1$ final state particles we can graphically represent it as in Figure 3.5(a), with the quark k and the gluon l being emitted at a small angle θ . Mathematically we have:

$$|\mathcal{M}_{n+1}|^2 d\Phi_{n+1} \rightarrow |\mathcal{M}_n|^2 d\Phi_n \frac{\alpha_S}{2\pi} \frac{dt}{t} P_{q,qg}(z) \frac{d\phi}{2\pi}, \quad (3.6)$$

where ϕ is the azimuth defined by \vec{k} and \vec{l} around the $\vec{k} + \vec{l}$ direction, z is an arbitrary parameter in general defined as a ratio between the energy of the particles emitted:

$$z = \frac{k^0}{k^0 + l^0}, \quad (3.7)$$

and t is the *hardness* parameter characterizing the divergence and the ordering of the splittings. It has the dimensions of a mass, and the preference is to take it as $t = E^2 \theta^2$. The values for ϕ , z and t are generated randomly during the Monte Carlo simulation process. The function $P_{q,qg}(z)$ is the Altarelli-Parisi splitting function, and is the only term that changes in Equation 3.6 between $q \rightarrow gq$, $g \rightarrow gg$ and $g \rightarrow q\bar{q}$ splittings.

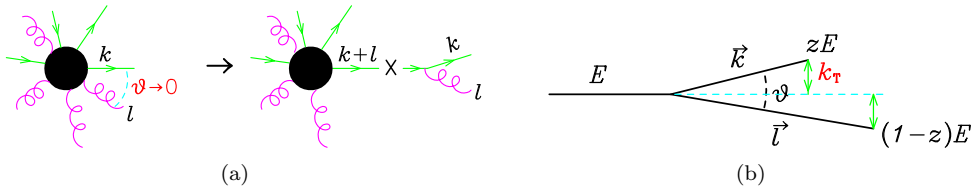


Figure 3.5: Left: graphical representation of the $q \rightarrow gq$ splitting. The black circles represent the \mathcal{M}_{n+1} and \mathcal{M}_n amplitudes of the tree-level processes. Right: kinematic of the splitting [22].

Factorization holds if the virtuality of the splitting parton $q^2 = (k + l)^2$ is negligible with respect to the energies entering the process, and can be applied iteratively as shown graphically in Figure 3.6. At this point, allowing for n splitting processes, the cross section can be written as:

$$\sigma_0 \frac{1}{n!} \alpha_S^n \log^n \frac{Q^2}{\lambda^2}, \quad (3.8)$$

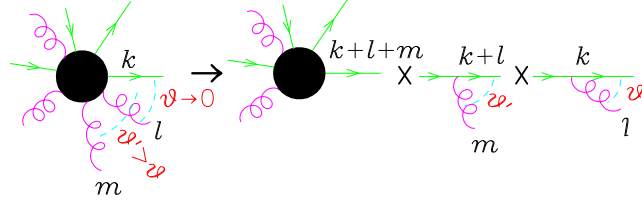


Figure 3.6: Recursive application of factorization, with the angles ordered as $\theta' \gg \theta \rightarrow 0$ [22].

where Q is the upper cut-off scale called *annihilation energy* that determines when the showering starts, and λ is the infrared cut-off. The shower ends when the virtuality q^2 reaches the *hadronization scale*, which is of the order of 1 GeV^2 . From the cross section expression of Equation 3.8, this procedure is called “leading log approximation”.

Once the shower is developed, the vertices and lines of the final configuration are assigned weights, which are for each vertex:

$$\theta(t - t_0) \frac{\alpha_S(t)}{2\pi} \frac{dt}{t} P_{i,jl}(z) dz \frac{d\phi}{2\pi}, \quad (3.9)$$

and for each line are the so-called *Sudakov form factors*:

$$\Delta_i(t', t'') = \exp \left[- \sum_{(jl)} \int_{t''}^{t'} \frac{dt}{t} \int_0^1 dz \frac{\alpha_S(t)}{2\pi} P_{i,jl}(z) \right] \quad (3.10)$$

where t' is the value of t at the upstream vertex, and t'' at the downstream vertex. If we reached the end of the graph, t'' is substituted by a cut-off t_0 . The Sudakov form factors specify the range of the z parameter for which the splitting is resolvable and represent the probability of *not* splitting. Figure 3.7 shows the typical graph shape of a shower evolved with splittings strongly ordered in angle.

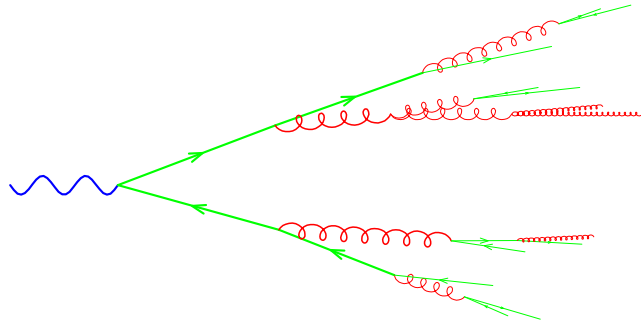


Figure 3.7: An example of a typical shower final graph [22].

Initial and final state radiation

We discussed up to now the development of parton shower arising from the emission from hadrons produced in the hard scattering, i.e. starting in general at an high annihilation scale Q^2 and progressively reaching the hadronization scale. This process goes under the name of *final state radiation* (FSR), as it is generated from outgoing partons of the hard interaction.

Parton shower can of course also happen before the hard interaction, and is called *initial state radiation* (ISR) as the incoming partons of the hard scattering originate the emission. In this case there is an important difference in the shower evolution, that is that the final energy of the showering is the hard interaction energy scale. To respect this fact, Monte Carlo simulation of ISR adopts a “backward evolution”, first setting the correct parton momentum distributions for the hard scatter, and then developing the shower backward, with the intermediate partons acquiring energy at each emission. The Sudakov form factors are then slightly different from Equation 3.10, being rescaled by a factor that takes into account the PDFs of the parton at the two vertices.

Matrix element and parton shower matching

So far, we introduced two powerful ways to describe a QCD event, one relying on our capability to compute the Matrix Elements (ME) in pQCD at the LO and NLO, the other exploiting a procedure to develop Parton Showers (PS) including soft and collinear emissions. ME can also introduce soft and collinear emissions, but the ME weight is in this case divergent, while in the PS scheme divergences are eliminated through the Sudakov form factors. We need therefore to set the rules to conveniently split the phase space of the event into two regions, one characterized by hard and large angle emission to be described by ME, the other of soft and collinear emission to be described by PS. This is achieved in the so-called “ME and PS matching”, where some resolution parameters are introduced with the role of soft and collinear cut-offs for ME.

The baseline idea is to compute the weight of an event using ME and then develop PS giving as inputs the ME weight as well as the event kinematics and color flow. A complication arises in this simple approach as the same final state can be obtained in multiple ways if ME and PS generated partons are swapped, as graphically shown in Figure 3.8, where the same event has three possible configurations. This issue goes under the name of “double counting”, and the matching scheme aim is to possibly avoid it or, at least, reduce its impact.

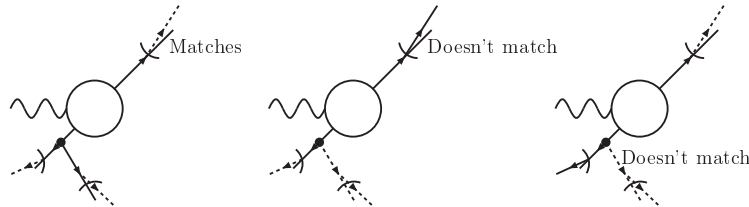


Figure 3.8: Example of double counting in hadron production. Dashed lines are PS emissions, solid lines are ME emissions. On the left, we have one hard large angle emission from ME and soft collinear emissions from PS. In the middle and on the right, one soft collinear emission from ME and both hard and soft PS emissions [22].

The main requirements on the matching scheme besides avoiding double counting are to perform a smooth transition from the ME and PS regions and to make sure the appropriate Sudakov form factors reabsorb the divergencies eventually introduced by the ME by reweighting the ME weight.

There are two main matching schemes: the Catani-Krauss-Kuhn-Webber (CKKW [23]) and the Michelangelo L. Mangano (MLM [24]) methods. They separate the phase space into the ME and PS regions by introducing resolution parameters that distinguish between *resolved* and *non-resolved* jets, to be described by means of the ME and PS respectively.

In the CKKW scheme, the parton-parton separation is measured by defining the distances between two final state partons and the distance between the parton and the beam using the k_\perp jet algorithm [25]. For a parton to be resolved, and described through ME, both variables have to be greater than a resolution parameter Y_{sep} . A branching tree is developed clustering together the two closest partons and ME elements are reweighted first to the strong coupling α_S value at the ME scale and then using a combination of Sudakov form factors. Then, PS is evolved and emissions at scales greater than Y_{sep} are vetoed, thus avoiding overlap between configurations.

In the MLM scheme, partons are first clustered into samples with different multiplicity and then, like in the CKKW method, the k_\perp jet algorithm is used to develop a branching tree and ME are reweighted to the proper strong coupling α_S value. At this point PS is performed and a jet finding algorithm matches partons into clusters. Jets with $p_T > p_{T_{\text{min}}}$, separation $R > R_{\text{min}}$ and pseudorapidity $\eta < \eta_{\text{max}}$ are considered for matching partons. Events are kept only if there is a one-to-one correspondence of partons to jets, else is rejected and thus double counting is avoided. As final step, the ME is reweighted with a Sudakov form factor.

The performance of the two matching methods has been extensively tested with data, and in particular it is important that the independence of the final result from the resolution parameters is verified.

3.2.3 Hadronization

When partons reach the hadronization scale energy $Q \sim 1$ GeV after showering, they recombine in bound colorless states according to the confinement principle, holding at low momentum. The so-called *parton-hadron duality* assumes that no high momentum transfer is needed in the recombination, as it happens close in phase space. This is a property of QCD experimentally observed, but there are no theoretical arguments explaining the hadronization. The solution is then to rely on phenomenological models.

The principle at the basis of hadronization models used in Monte Carlo is the *large N_c limit*, or *planar limit*, where N_c is the number of colors and we consider the QCD value $N_c = 3$ as just the dominant contribution. Simple rules are then defined: color and anticolor indices go from 1 to N_c ; quark and antiquark lines are oriented and assigned a color and anticolor index respectively; gluon lines are oriented and assigned a pair of color-anticolor indices to achieve color neutrality. The color structure of the three splitting processes according to these rules are shown in Figure 3.9(a). While the assignment of color connections in the case of $q \rightarrow qg$ and $g \rightarrow q\bar{q}$ splittings is univocal, for $g \rightarrow gg$ there are two possible configurations (where by inverting the two final state gluons transform one into the other) and when the

color connections are reconstructed they are chosen with a 50% probability each. The final picture looks e.g. like the graph in Figure 3.9(b), where the important information is not the specific color assigned to the final state parton, but rather the *color flow*.

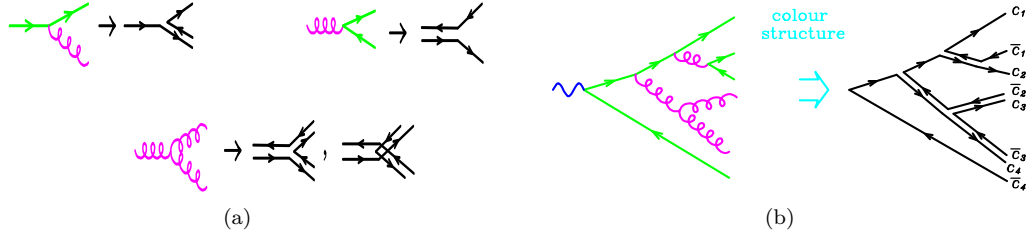


Figure 3.9: Left: rules to assign color connections in the splittings $q \rightarrow qq$ (top left), $g \rightarrow q\bar{q}$ (top right) and $g \rightarrow gg$ (bottom). Right: example of a color connected shower [22].

At this point, two possible phenomenological fragmentation models come in the game to bound partons into hadrons starting from the color connected final state. They both have been tuned using collider measurements over the last decades to properly describe the final state hadron multiplicity and need in general a large number of parameters.

The first hadronization scheme is called *Lund string model* and ties a quark with an antiquark plus a number of intermediate gluons, like stretching a string (or a “color flux tube”) from the quark to its color-connected antiquark taking in the gluons that lie inbetween them. This can be seen as an illustration in Figure 3.10(a) and Figure 3.10(b): the first string collects the quark with color c_1 , the antiquark with color \bar{c}_4 and all the final state gluons along the path. It uses string dynamics to describe the color flux between quarks. In other words, the string between the quark and antiquark produces a linear confinement potential.

The other hadronization scheme is the *cluster model*, where final state gluons are forced to split into a quark-antiquark pair and then color connected quark-antiquark pairs are bounded together. Figure 3.10(c) presents a graphical illustration of the concept. Because of *preconfinement* (the fact that color connected pairs with large invariant masses are Sudakov suppressed in angular ordered showers) the cluster can be associated with an hadronic two-body system.

During the last decades, different measurements at colliders have been used to tune these models to properly describe the hadron multiplicity in the final state.

3.2.4 Underlying event

With “underlying event” (UE) we refer to the secondary parton interactions at low transferred momentum that accompany the main hard process. The underlying event is flavor- and color-connected to the hard scattering and in real data is in general not separable from the event of interest. It is typically observed as jets of particles close to the direction of the beam and cannot be modeled with perturbative QCD but is instead studied from experimental data on *minimum bias* events at low momentum.

Besides a backward shower modeling starting from the beam remnants, an important contribution to the underlying event are multiple parton interactions, i.e. secondary relatively hard collisions between the incoming hadron remnants. Phenomenological models are

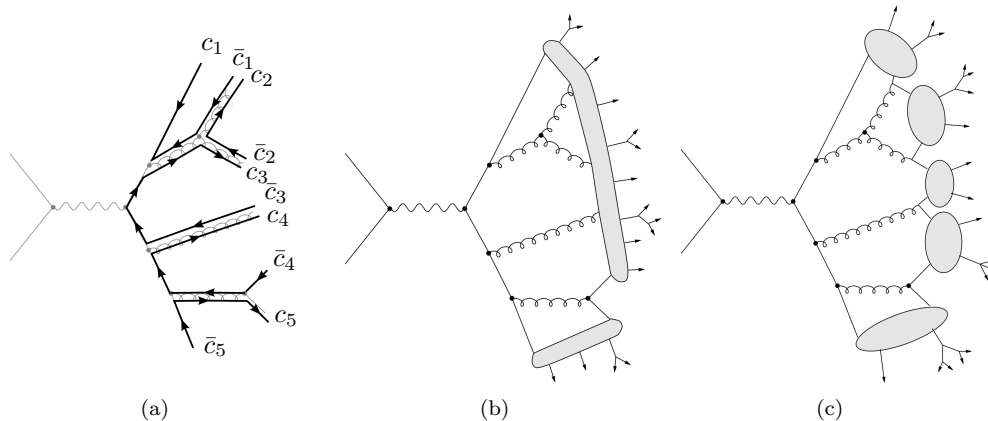


Figure 3.10: Drawing of a color connected parton shower graph (a) completed with hadronization from the Lund string model (b) and the cluster model (c) [20].

used to simulate the underlying event, and additional semi-hard interactions are generated with different primary vertices to account for the effect of pile-up.

3.3 Generators

Monte Carlo generators can either be *multi-purpose* generators, i.e. capable of performing the full simulation chain described in this chapter, or *specialized* generators, i.e. devoted to a single aspect of the simulation. As should be clear after the discussion about the modeling of hadronic collisions, there are some choices to be done that might result being better suited for some particular events or others. Therefore the Monte Carlo generators should be chosen according to their performance in modeling the event of interest.

We briefly present in the following sections the main characteristics of the generators that are used in the analyses that are the object of this dissertation.

PYTHIA

PYTHIA [26] is a multi-purpose Monte Carlo generator using ME computed at LO for $2 \rightarrow n$ ($n \leq 3$) events and PS with emissions ordered in p_T instead of angle. The Lund string model is used for hadronization and UE simulation is included. Minimum bias events with $p_T > \hat{p}_{Tmin}$ are used to model interactions between proton remnants.

HERWIG

HERWIG [27] is a multi-purpose Monte Carlo generator using ME computed at LO for $2 \rightarrow 2$ events and PS with emissions ordered in angle. The cluster model is used for hadronization and for the UE description, HERWIG is typically interfaced with the external package JIMMY [28] which simulates UE as scattering between proton remnants in $2 \rightarrow 2$ ME computed at LO.

ALPGEN

ALPGEN [29] is a Monte Carlo generator specialized for ME computation of $2 \rightarrow n$ ($n \leq 9$) events at LO, with cross sections computed using the ALPHA algorithm [30]. It is interfaced either with PYTHIA or HERWIG for PS development and ME/PS matching is done in the MLM scheme, where the resolution parameter $p_{T_{\min}}$ is called *jet matching scale*. Hadronization and UE are simulated through HERWIG and hence JIMMY.

The various parton multiplicity samples are then normalized to their LO cross section and combined into an inclusive sample, which is finally typically normalized to an inclusive cross section calculated at higher order in pQCD. For the inclusive production of Z and W bosons in p-p collisions, the MCFM [31] and FEWZ [32] programs are used to predict cross sections at NLO and NNLO respectively.

MC@NLO

MC@NLO [33] is a Monte Carlo generator simulating ME at NLO, where the use of 1-loop corrections introduce the possibility of having negative weighted events. Theoretical uncertainties on the inclusive cross section is reduced thanks to the use of full NLO corrections, but higher multiplicity parton emission is simulated through PS in HERWIG which has a poorer description of hard emissions. Hadronization and UE are also simulated through HERWIG (and hence JIMMY).

SHERPA

SHERPA [34] is a multi-purpose Monte Carlo generator interfaced with PYTHIA for the parton shower. ME/PS matching is performed with the CKKW scheme. A modular design for SHERPA allows for simple implementation of other techniques, e.g. NLO corrections can be introduced in the CKKW matching scheme using a NLO Monte Carlo generator with the MENLOPS procedure [35]. Hadronization is done within PYTHIA and a multiple parton scattering model for UE simulation.

POWHEG

POWHEG [36] is a Monte Carlo generator computing ME at NLO and typically interfaced either with PYTHIA or HERWIG for the modeling of PS, hadronization and UE.

MADGRAPH

MADGRAPH [37] is a Monte Carlo generator specialized for ME computation of $2 \rightarrow n$ ($n \leq 6$) events at LO interfaced with PYTHIA for the modeling of PS, hadronization and UE.

ACERMC

ACERMC [38] is a Monte Carlo generator computing ME at LO and typically interfaced either with PYTHIA or HERWIG for the modeling of PS, hadronization and UE.

3.4 ATLAS detector simulation

Events generated with Monte Carlo simulation can be directly used at *parton level*, i.e. without any further operation on the generated partons, or be reconstructed either at *truth level*, where the particles go through object reconstruction (see Chapter 4) without interacting in the detector material and the original kinematics is maintained, or go through detector simulation [39] and after that through object reconstruction, to obtain the so-called *reconstructed level*.

The detector material, geometry and response are modeled using the **GEANT4** [40] package. The interaction of particles with ATLAS subsystems is converted into detector signals of the same sort of the real read-out and at this point the same kind of reconstruction algorithms shape the detector output into physical objects. During test-beam periods the **GEANT4** parameters have been tuned to best simulate the ATLAS configuration and the performance of detector simulation has been extensively checked also with data calibrations.

The detector simulation relies on the usage of two databases: the *geometry database* contains the information on the detector volumes like dimensions, geometry, position and material composition, while the *conditions database* is constantly updated with the information on the real detector real-time conditions as dead channels, misalignments, temperature. Since conditions vary from run to run, it is important that the detector simulation reproduces as close as possible the real status of ATLAS during a particular data period. Also for this reason, Monte Carlo samples are regularly reproduced consistently with *data reprocessings* or *data releases*. For the analyses presented in this dissertation, the Monte Carlo production tagged as **mc12** is used, performed within release 17 of the ATLAS analysis framework **ATHENA** [?].

3.5 Monte Carlo samples corrections

At the end of the full Monte Carlo simulation chain, after the detector simulation and event reconstruction steps, the generated samples need some corrections to better model data. The main event reweighting is to correct Monte Carlo samples to the correct theoretical cross section of the process and to the number of expected data events, which comes from the luminosity measurements. As typical in Monte Carlo techniques, an higher number of randomly produced events assures a better modeling of the system under study, and therefore usually a very high number of events are produced for each sample to maximize the confidence that all the relevant configurations have been copiously simulated. The event weight w to be applied (event by event) is defined as:

$$w = \frac{\sigma \times k}{N} \int \mathcal{L} dt, \quad (3.11)$$

where σ is the process theoretical cross section, N is the number of Monte Carlo events, $\int \mathcal{L} dt$ the integrated luminosity and k is the so-called k -factor, which is a correction to higher orders as, e.g., to bring the accuracy of a LO cross section computation to the NLO.

Furthermore, a weight to account for pile-up effect is to be applied, to match the expected number of interactions per bunch crossing $\langle \mu \rangle$ in real data-taking conditions.

830 Event reconstruction

831

832 After having described the ATLAS detector in Chapter 2 and the procedure for Monte
 833 Carlo simulation of events in Chapter 3, we understand that what we deal with when we talk
 834 about “data” is raw digital signals from the detector, either the real one or the simulated
 835 one.

836 In the following Chapter we will explain how, starting from these outputs, objects are
 837 reconstructed to be used in physics analyses [41]. This process is what is called “offline event
 838 reconstruction” since it is not done in real time, due to the time required by the algorithms
 839 to perform their tasks.

840 In general we could describe the full procedure as subdivided into three main steps: a
 841 pre-reconstruction stage where the electronic signals are translated into measurements; a
 842 pattern-recognition step where the measurements are assembled into the building blocks of
 843 particles, e.g. tracks and energy clusters; a particle identification final leg where the full
 844 detector information elaborated is combined to match a candidate physics object (electrons,
 845 muons, jets and the missing transverse energy E_T^{miss}).

846 The expected signatures for the various particles in terms of interaction with the detector
 847 system are schematically shown in Figure 4.1.

848 4.1 ID Tracks

849 Particle trajectories (“tracks”) are used both to reconstruct the particle itself, giving the
 850 momentum measurement, and to identify the interaction vertices. The parameters describing
 851 a track are: q/p , the charge divided by the momentum; θ , or more used η , the angle with
 852 respect to the Z axis in the RZ plane measured from the perigee¹; ϕ_0 , the angle with respect
 853 to the X axis in the XY plane measured from the perigee; d_0 , the impact parameter, or
 854 perigee with respect to the Z axis in the XY plane; z_0 , Z component of the perigee. These
 855 parameters are shown in the double-view drawing of Figure 4.2.

856 In order to reconstruct the track, the first step is to retrieve the information from the
 857 ID hits, which are converted into three-dimensional space points. Then, the *inside-out*

¹The perigee is the point of the track closest to the origin.

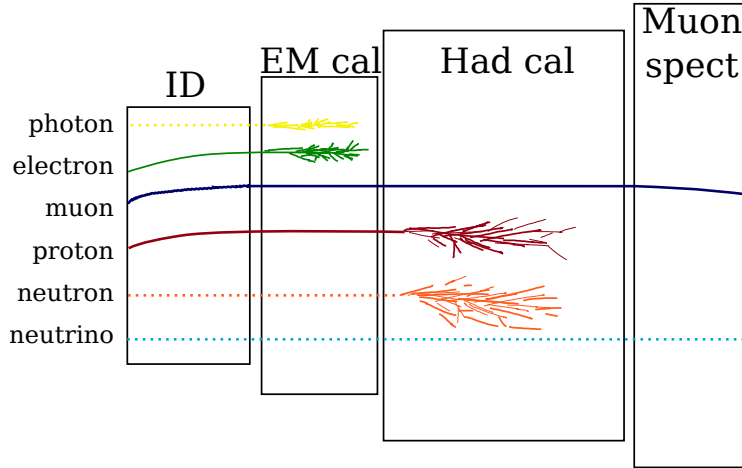


Figure 4.1: Drawing illustrating how particles are detected in the ATLAS sub-systems.

algorithm [42] is used, starting from a seed of three aligned hits in the pixel detector or in the SCT. From there, a path is formed along the seed directional information adding space points one by one. This is done by using a Kalman filter algorithm [43] which checks progressively the compatibility between the track (also progressively updated) and the new point. The five track parameters described before are also computed at this step. A cleaning procedure then rejects incomplete tracks or tracks sharing hits with others, or composed by false space points. The candidate tracks are extended into the TRT and re-fitted taking into account the effects from the interaction of the charged particle with the detector material.

A second algorithm, called *outside-in*, is applied in order to better reconstruct tracks from secondary charged particles. This algorithm does the opposite of the inside-out one, taking as seeds hits in the TRT (the ones not associated to any track candidate in by the inside-out reconstruction) and extrapolating back to the SCT and pixel detector.

4.2 Primary vertices

In general, a primary vertex (PV) is identified by the tracks associated to it. The reconstruction is performed via an iterative procedure [44] starting from a seed defined as the maximum in the distribution of the z_0 parameter of reconstructed tracks. After tracks are assigned to the PV with the aid of an iterative χ^2 fit, the ones that fall out of more than 7σ from the PV are used to seed another PV until no track is left without being assigned to a vertex (one track can be associated to more than one vertex).

A PV must have at least two associated tracks and its position must be consistent with the beam collision region in the XY plane. The hard-scatter PV is chosen as the one with the highest sum of squared transverse moments of the tracks. The other reconstructed PVs are identified with pile-up interactions. Another kind of vertices, not compatible with the requirement of coming from close to the proton collision spot, are the secondary vertices, originating from the decay of short-lived particles. These vertices are useful to identify B -hadrons and will be described in Section 4.6.2.

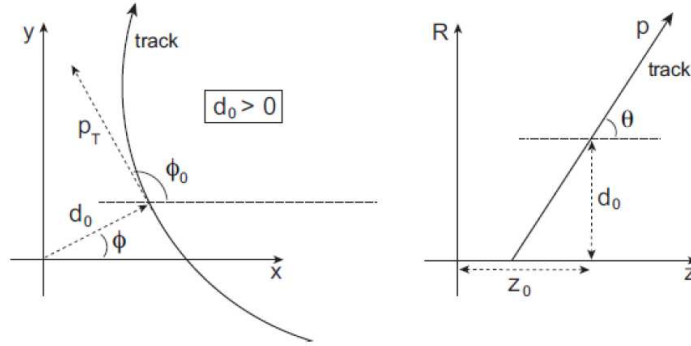


Figure 4.2: Schematic drawings of the parameters used for track reconstruction in the XY and RZ planes (left and right respectively) where the origin is the beam spot, i.e. where the protons collide and interact.

884 As can be expected, high pile-up environments deteriorate the performance of vertex
 885 reconstruction, as more fake tracks are introduced and nearby interaction might lead to the
 886 misreconstruction of distinct vertices as a single one [45].

887 4.3 Energy clusters

888 With the name “energy cluster” we generically refer to energy deposits in the calorimeter
 889 cells that are grouped together on the basis of some criteria [46]. In particular, we are
 890 interested in *topological clusters* and *electromagnetic towers*, used respectively for jets and
 891 electron/photon reconstruction.

892 Topological clusters, abbreviated as “topoclusters”, are built from neighboring calorime-
 893 ter cells starting from a seed deposit with a signal (S , the cell measured energy) to noise
 894 (N , the RMS of the cell noise distribution) ratio higher than a certain threshold. Cells with
 895 $S/N \geq 4$ are taken as seeds, and starting from the one with the highest S/N all the neigh-
 896 boring cells with $S/N \geq 2$ are added to the topocluster. Topoclusters are treated as massless
 897 and their energy at the electromagnetic scale is the sum of the constituent cells. Their po-
 898 sition and direction parameters are obtained from a weighted sum of the constituent cells’
 899 pseudorapidity and azimuth angle based on the absolute value cell’s energy. Since energy
 900 measurement can be negative (due to noise fluctuations), clusters with negative energies are
 901 rejected.

902 Towers are built using the *sliding window* algorithm [47] starting from single energy
 903 deposits in the EM calorimeter middle layer of size $\Delta\eta \times \Delta\phi = 0.025 \times 0.025$. As schematically
 904 shown in Figure 4.3, a window of 3×5 cell units is defined, centered on the maximum of
 905 energy and finally expanded to optimize the cluster reconstruction, with a size that depends
 906 on the object (electron or photon) and the position in the detector (3×7 in regions with
 907 $|\eta| < 1.4$ and 5×5 elsewhere).

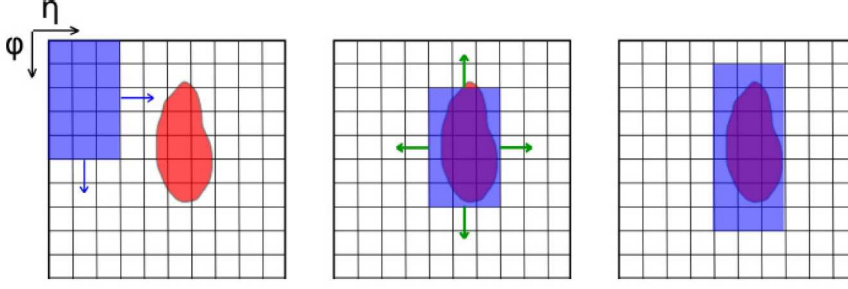


Figure 4.3: The three steps of the sliding window algorithm.

4.4 Electrons

Electrons [47] are reconstructed for pseudorapidities up to $|\eta| = 2.47$, where information from the ID is available, matching a track (see Section 4.1) with a cluster in the electromagnetic calorimeter reconstructed with the sliding window algorithm (see Section 4.3). In order to account for bremsstrahlung losses the matching is done within a region of dimension $\Delta\eta \times \Delta\phi = 0.05 \times 0.10$ and if more candidate tracks are matched, of all the ones with hits in the silicon detectors the track with the smallest ΔR with respect to the energy cluster is chosen. In addition, the track momentum has to be compatible with the cluster energy, which is calibrated to the electromagnetic scale derived from Monte Carlo based corrections (to account for dead material losses), test-beam studies and calibration from $Z \rightarrow ee$ events [48].

In general, electron can be distinguished from hadrons thanks to various characteristics of their shower development: electrons deposit the most of their energy in the second layer of the EM calorimeter; the width of their shower is narrower; they have smaller hadronic leakage²; the E/p variable (ration of cluster energy and track momentum) is higher.

Some difficulties arise when dealing with π^0 and η particles, which decay into two γ s that produce two close showers reconstructed as a single one in the second layer of the EM calorimeter, and in general with jets faking electrons from, e.g. QCD processes. There are then six different electron definitions to help separate real electrons from fake ones, described in the following ordered from the looser requirements to the tightest. Performance studies on electron reconstruction and identification were done using 2010 data and Monte Carlo $Z \rightarrow ee$ and $W \rightarrow e\nu$ events [47] (see Figure 4.4).

Loose electrons lie in the pseudorapidity region $|\eta| < 2.47$ and have low hadronic leakage and requirements on the variables defining the shower shape. The identification efficiency is high but the jet rejection is low (about 500).

Loose++ electrons are **loose** electrons whose track has at least one hit in the pixel detector and at least 7 hits in the combined silicon detectors and the $|\eta_{\text{firstEM}}|$ distance between the track extrapolated to the first EM layer and the matched cluster is lower than 0.015. The identification efficiency is similar to the loose one but the rejection is ten times

²The hadronic leakage is the ratio of the transverse energy reconstructed in the first layer of the hadronic calorimeter to the total transverse energy reconstructed in the EM calorimeter.

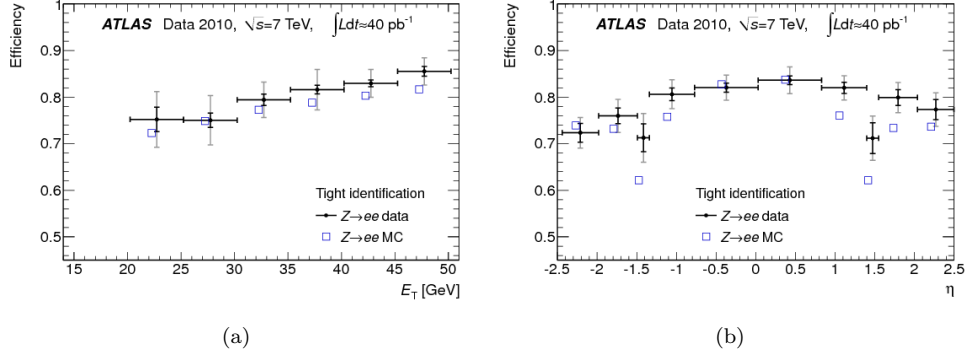


Figure 4.4: Tight electron identification efficiencies measured from $Z \rightarrow ee$ events and predicted by MC as a function (left) of E_T (integrated over $|\eta| < 2.47$ excluding the transition region $1.37 < |\eta| < 1.52$ and (right) of η and integrated over $20 < E_T < 50$ GeV. [47]

higher.

Medium electrons are `loose++` electrons where additional requirements on shower shape are made as well as on their tracks: $|d_0| < 5$ mm and $|\eta_{\text{firstEM}}| < 0.01$. The efficiency drops to 88% and the rejection is higher than the previous.

Medium++ electrons are `medium` electrons whose track has at least one hit in the first pixel detector layer, a requirement that allows to reject electrons from photon conversion. Charged hadrons contamination is reduced by discarding candidates whose track has a low fraction of high-threshold TRT hits. In addition, $|\eta_{\text{firstEM}}| < 0.005$ and stricter cuts are applied to shower shaper of clusters in $|\eta| < 2.01$. The efficiency is about 85% and rejection is about 50×10^3 .

Tight electrons are `medium++` electrons with additional requirements on the distance between the track and the matched cluster ($|\Delta\phi| < 0.02$, $|\Delta\eta| < 0.005$) and on the E/p variable. Stricter cuts are imposed on the fraction of high-threshold TRT hits and on the impact parameter ($|d_0| < 1$ mm). The efficiency drops to 75% and the rejection is higher than the previous one.

Tight++ electrons are `tight` electrons with asymmetric $\Delta\phi$ cuts, which give both better efficiency and rejection.

4.4.1 Additional requirement and corrections for analyses

For our analyses [49], electrons in the transition region $1.37 < |\eta_{\text{cluster}}| < 1.52$ with inactive material are excluded. Electrons are required to satisfy `tight++` criteria and to have $E_T = E_{\text{cluster}} / \cosh \eta_{\text{track}} > 25$ GeV and $z_0 < 2$ mm. In addition, to suppress further the QCD multijet background, isolation cuts are imposed both as calorimeter (using the energy in a cone of size $\Delta R < 0.2$, `EtCone20`) and track isolation (using the scalar sum of p_T s from tracks within a cone of $\Delta R < 0.3$, `PtCone30`). The `EtCone20` and `PtCone30` isolation cuts are chosen to give 90% efficiency. In addition, jets (see Section 4.6) within $\Delta R = 0.2$ of the selected electron are discarded, and if an additional jet with $p_T > 25$ GeV and $|JVF| > 0.5$ is found within $\Delta R = 0.4$, then the electron is rejected. The electron is

matched to the single electron trigger `EF_e24vhi_medium1` combined with a logical OR to the `EF_e60_medium1` trigger, which recovers some efficiency loss at $E_T > 80$ GeV.

The efficiency in selecting electrons can be factorized as:

$$\varepsilon = \varepsilon_{\text{reco}} \cdot \varepsilon_{\text{tight++}} \cdot \varepsilon_{\text{isolation}} \cdot \varepsilon_{\text{trigger}} \quad (4.1)$$

where the various components represent respectively: the efficiency in reconstructing the electron in terms of track-cluster match, track quality and hadronic leakage; the efficiency for the `tight++` identification criteria; the efficiency for the isolation cuts; the efficiency from trigger selection. Scale factors are derived in bins of (η, E_T) , and the trigger scale factors are separated into four data-taking periods (A-B3, B4-D3 without C1-C5, C1-C5 and D4+). The efficiency scale factors are applied as weights to Monte Carlo events.

The electron energies in data are corrected using scale factors $\alpha(\eta)$ derived from data-to-simulation comparison in $Z \rightarrow ee$ events in order to match the Z boson mass peak.

4.5 Muons

As suggested in Figure 4.1, muons interact with all of ATLAS sub-detectors, even though they act as minimum ionizing particles (mip) for the calorimeters and hence will deposit only a very small fraction of their energy in the material. Their track instead is precisely measured both in the ID and in the muon spectrometer (MS). Based on how we decide to combine the various information, we can list the following types of reconstructed muons: `standalone` muons take the MS track and extrapolate it back to the interaction point; `combined` muons match the MS track with the tracks from the ID; `segment tagged` muons extrapolate ID tracks to the spectrometer and match the result with MS segments; `calorimeter tagged` muons extrapolate ID tracks to the calorimeters and match the result with energy deposits.

We will only consider `combined` muons, reconstructed using an algorithm called `Muid` [50] and whose pseudorapidity is limited to $|\eta| < 2.5$ by the ID acceptance. Starting from $\Delta\eta \times \Delta\phi = 0.4 \times 0.4$ regions where interesting activity has been triggered, track segments are searched for in the RPC and TGC and combined into a single track by means of a least-square fitting method. These track candidates are hence extrapolated back to the interaction point and their momentum corrected for the mip energy loss in the calorimeter material.

At this point a χ^2 test (checking the difference between the extrapolated track coordinates weighted with combined covariance matrix) on the matching of the candidate MS track and the tracks reconstructed in the ID is performed to obtain the final muon candidate track. Only ID tracks that satisfy some quality requirements are considered for the matching: they need to have at least two pixel hits, of which at least one in the first layer; at least two pixel hits plus number of crossed dead pixel sensors; at least six SCT hits plus number of crossed dead SCT sensors; maximum two pixel or SCT holes³; defining the number of TRT outliers⁴ and the number of TRT hits as N_{TRT_o} and N_{TRT_h} respectively, $N_{\text{TRT}_h} > 5$ and $N_{\text{TRT}_o}/N_{\text{TRT}_h} < 0.9$ for $|\eta| < 1.9$, $N_{\text{TRT}_o}/N_{\text{TRT}_h} < 0.9$ if $N_{\text{TRT}_h} > 5$ for $|\eta| \geq 1.9$. In

³A “hole” in the silicon detectors is a region where the module did not perform as expected even though the surrounding ones did.

⁴“Outlier” is an hit that is deviated from the track path.

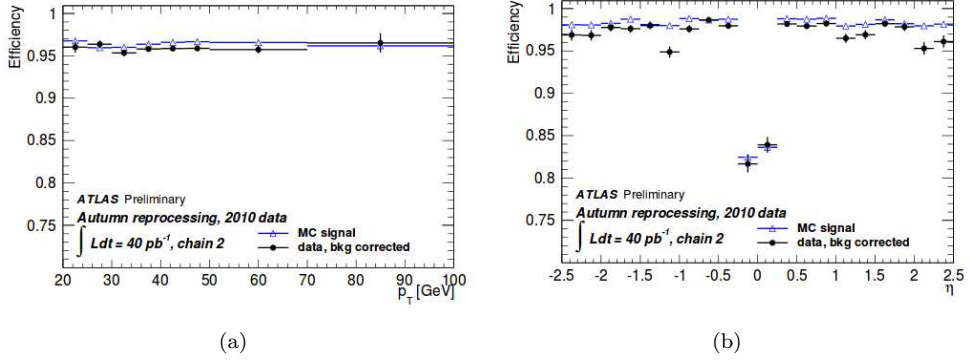


Figure 4.5: Combined muon reconstruction efficiencies using the Muid algorithm measured from $Z \rightarrow \mu\mu$ events and predicted by MC as a function (left) of p_T and (right) of η . [50]

case no matching is found, no muons are reconstructed, while if more candidates arise, the one giving the best χ^2 is chosen. The momentum is computed as a weighted average of ID and MS measurements.

Performance studies on muon reconstruction and identification were done using 2010 data and Monte Carlo $Z \rightarrow \mu\mu$ events [50] (see Figure 4.5).

4.5.1 Additional requirement and corrections for analyses

Combined muons are used in our analyses [49] with an additional cut on the longitudinal impact parameter $|z_0| < 2$ mm to ensure the track comes from the hard-scattering primary vertex. A requirement on the muon momentum of $p_T > 25$ is used to obtain 90% efficiency from the chosen single muon trigger, which is the logical OR combination of the triggers EF_mu24i_tight and EF_mu36_tight. The EF_mu24i_tight trigger includes an isolation requirement for which the p_T sum of the tracks in a cone of size $\Delta R = 0.2$ around the muon has to be less than the 12% of the muon transverse momentum. Muons overlapping with any jet (see Section 4.6) with $p_T > 25$ GeV and $|JVF| > 0.5$ within a $\Delta R < 0.4$ cone are rejected.

In addition to the previous isolation requirements, a “mini-isolation” is defined [49] to better deal with the high pile-up present in $\sqrt{s} = 8$ TeV collision events. The mini-isolation is defined as

$$I_{mini}^l = \sum_{tracks} p_T^{track} / p_T^l \quad (4.2)$$

where p_T^l is the lepton transverse momentum and the summation runs over all tracks found in a cone whose radius varies as a function of the muon momentum as:

$$\Delta R(l, track) = \frac{10 \text{ GeV}}{p_T^l}. \quad (4.3)$$

The tracks also have to satisfy: $p_T^{track} > 1$ GeV; $d_0 < 10$ mm; $z_0 \sin \theta_{track} < 10$ mm; at least four hits or dead sensors crossed in the silicon detectors. The cut on the mini-isolation variable is chosen as $I_{mini}^l < 0.05$. The performance of the mini-isolation is shown

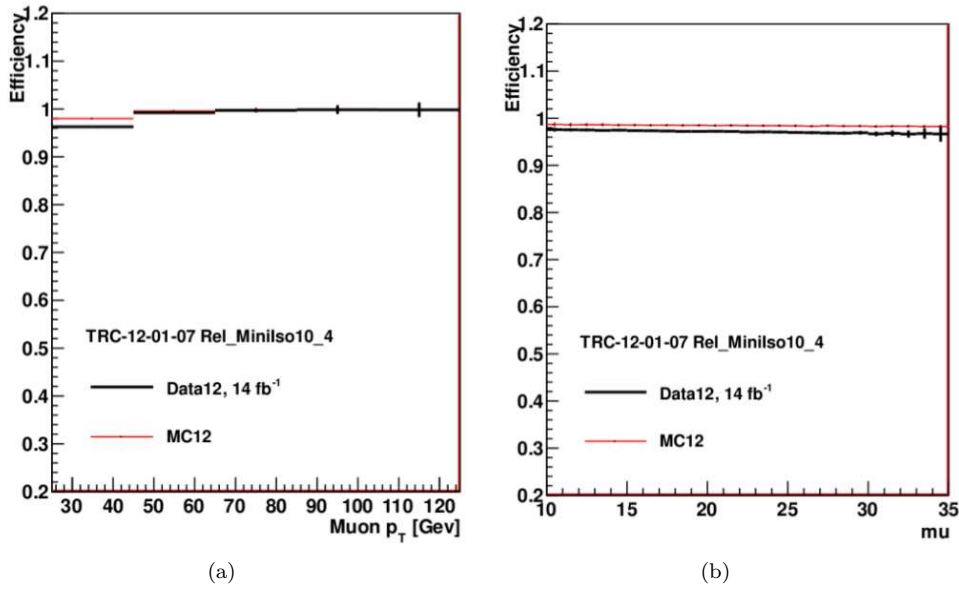


Figure 4.6: Efficiency of the mini-isolation as a function of the muon momentum (left) and of the average number of bunch crossings $\langle \mu \rangle$ (right) [49].

in Figure 4.6.

As is done for electrons, a set of corrections are applied to correct for minor discrepancies between Monte Carlo simulation and data events. The scale factors to compensate reconstruction, isolation and trigger inefficiencies are derived from tag-and-probe measurements and applied to Monte Carlo events. In addition, the muon momentum in simulated events is smeared to obtain agreement between the momentum resolutions in Monte Carlo and data.

4.6 Jets

With the name “jet” we generically refer to the object formed as a consequence of parton hadronization from a spray (or *jet*) of particles. These particles will leave signals both as tracks in the ID and as energy deposits in the calorimeters and two type of jets can then be defined using either the former or the latter information: track jets and calorimeter jets. In the following, we will only deal with calorimeter jets.

In order to interpret the detector information, first topoclusters are formed from the calorimeter cells signals, as explained in Section 4.3. Then, different algorithms were developed to associate topoclusters into a jet. Because of the need for a stable and precise performance over the QCD processes from p-p collisions, a set of requirements has been defined for the algorithms to be valid [51].

First of all, the splitting of one particle into two collinear particles must not change the result of the algorithm reconstruction, as well as the presence of additional soft emission. The importance of Infrared and Collinear (IRC) safety is evident considering e.g. that a hard parton, as part of the fragmentation process, will undergo many collinear splittings, and that QCD events always include emission of some soft particles, perturbatively or not. In addition, we want the algorithm result to be invariant under Lorentz boost along the

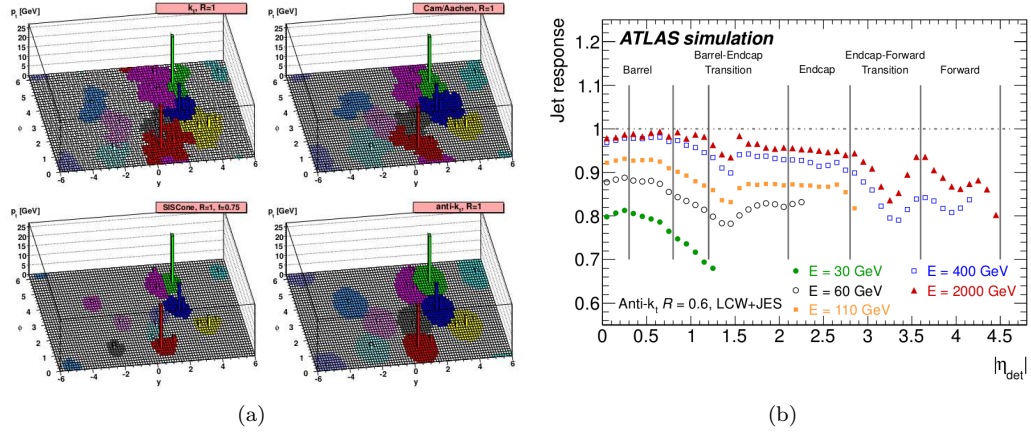


Figure 4.7: Left: The same input produces different results in terms of jet reconstruction using various jet algorithms [51]. Right: Average jet energy response from simulated events at the LCW scale for various calibrated energies (E) as a function of pseudo-rapidity. The inverse of the response shown in each bin is equal to the average jet energy scale correction [55].

1041 beam direction, to be as insensitive as possible to detector effects like noise or resolution,
1042 and to be light in terms of computing resource usage.

A set of jet algorithm that satisfy these requirements are the sequential recombination algorithms [52, 53, 54], which combine topoclusters into jets using as criteria a distance parameter defined as:

$$d_{ij} = \min(p_{T_i}^{2p}, p_{T_j}^{2p}) \frac{\Delta R_{ij}^2}{R^2}, \quad (4.4)$$

$$d_i = p_{T_i}^{2p}, \quad (4.5)$$

where p_{T_i} is the transverse momentum of topocluster i , $\Delta R_{ij} = \sqrt{\Delta\eta^2 + \Delta\phi^2}$ the distance between constituents i and j , R a parameter of the algorithm that approximately controls the size of the jet, p the parameter that defines the type of algorithm as:

$$\begin{aligned} p = 1 & : k_t \text{ algorithm;} \\ p = 0 & : \text{Cambridge/Aachen algorithm;} \\ p = -1 & : \text{anti-}k_t \text{ algorithm.} \end{aligned} \quad (4.6)$$

1043 The algorithms compute d_{ij} , the distance between the two topocluster inputs i and
1044 j , and d_i , the distance between the input i and the beam axis in the momentum space.
1045 By computing the minimum of the two distances the choice made is to combine i and j
1046 into a new input if $d_{ij} < d_i$, or take i as a jet candidate and remove it from the input
1047 list if $d_i < d_{ij}$. The cluster combination is done by summing the four-momentum of each
1048 input. The distances are recalculated with the updated list of input objects and the process
1049 repeated until no further cluster is left.

1050 The anti- k_t algorithm is chosen by most of analyses in ATLAS as it is particularly
1051 performant against pile-up, since it starts summing up constituents with higher momentum,
1052 and produces jets with a conical structure (see Figure 4.7(a)).

4.6.1 Additional requirement and corrections for analyses

For our analyses [49] jets are reconstructed using the anti- k_t algorithm with a radius parameter $R = 0.4$ (from which the algorithm is often referred to as anti- k_t4) using calorimeter energy deposits corrected for effects of non-compensation⁵, dead detector material and out-of-cluster leakage. Other effects affecting jet energy are low momentum particles that are deflected by the magnetic field and energy losses in topocluster formation and jet reconstruction [55].

The initial energy is reconstructed at the electromagnetic (EM) scale as the calorimeter signals arise from electromagnetic interaction of particles with matter. The energy calibration to EM scale was derived during test-beam runs using electron beams, validated with muons from both test-beam and cosmic-rays runs and corrected using simulated $Z \rightarrow ee$ events.

Of the several energy calibration schemes derived in ATLAS, we will be using the Local Cluster Weighting (LCW) calibration [56, 57]. This scheme exploits properties of the topoclusters shapes to classify the clusters as “mainly electromagnetic” or “mainly hadronic” and then derives the calibration from Monte Carlo simulation of charged and neutral pion events. The calibration corrections are applied before the jet reconstruction algorithm is operated, and after the jet is formed a final correction is applied to ensure linearity in response.

In our analyses we consider only jets with $p_T > 25$ GeV and $|\eta| < 2.5$. Furthermore, a variable called “jet vertex fraction” (JVF) is defined as the fraction of the sum of p_T of tracks with $p_T > 1$ GeV associated with the jet that comes from tracks originating from the primary vertex. By requiring $JVF > 0.5$ we avoid selecting jets from in-time pile-up events.

To avoid double counting of energy deposits from electrons as jets, if jets are found within ΔR of 0.2 of the selected electron, the jet closest to the lepton is removed and then electrons that lie within $\Delta R < 0.4$ of the remaining jets are discarded.

4.6.2 b -tagging

When a bottom quark is produced in an events, it hadronizes into a B hadron, which has a lifetime of the order of 10^{-12} s and hence can travel about 3 mm before decaying. The result is a displaced secondary vertex that, if correctly reconstructed, can allow for the identification of the bottom quark. Since this capacity relies on track reconstruction from the ID, its applicability is limited by the ID acceptance to the pseudorapidity region $|\eta| < 2.5$.

This technique is called b -tagging [58] and is widely used in ATLAS analyses with top quarks. There are three types of algorithms, and they can be combined to obtain better performance. In general they define a weight corresponding to the probability for the jet to be tagged, and a working point is chosen as the threshold for this weight to discriminate between b - and not- b -jets by finding a good compromise between a good efficiency (the ratio between tagged b -jets and true b -jets) and a high light-jet rejection (the inverse of the number of light-jets misidentified as b -jets).

⁵The energy response to hadrons is lower than the response to electrons of the same energy due to the presence of invisible processes.

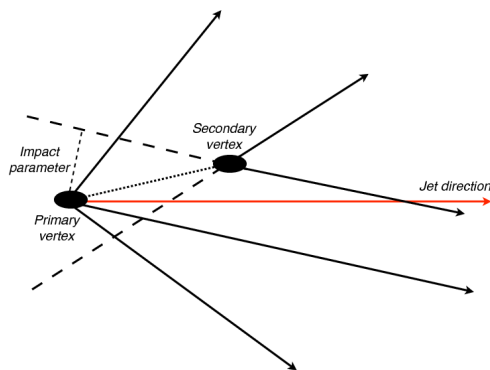


Figure 4.8: Simple schematic of the displaced secondary vertex.

1094 Algorithms like IP1D, IP2D and IP3D are based on information from impact parameters
 1095 of the tracks contained in the jet, z_0/σ_{z_0} , d_0/σ_{d_0} and a combination of the two respectively.
 1096 A likelihood is computed to obtain the b -tag weights.

1097 Other algorithms reconstruct the secondary vertex from the B hadron decay, allowing
 1098 for a better discrimination between b -jets and light jets. The SV1 algorithm uses the number
 1099 of track pairs in the secondary vertex, their total invariant mass and the ratio of the sum
 1100 of the energies of tracks from the secondary vertex to the one of the total tracks of the jet
 1101 to compute likelihood ratios the logarithm of which are then summed to obtain the b -tag
 1102 weights.

1103 Finally, the `JetFitter` algorithm uses the full decay chain reconstruction of b and c
 1104 hadrons by fitting it with a Kalman filter to determine a common path between the primary
 1105 vertex and the vertices from the b and c hadrons inside the jet. The likelihood is computed
 1106 with the flight length significances of the vertices and the variables from the SV1 algorithm.

1107 The algorithm employed in our analyses is called `MV1` and uses a neural network to
 1108 combine information from the `JetFitter`, IP3D and SV1 algorithms. The working point
 1109 corresponding to 70% efficiency, ~ 130 light-jet rejection and a charm-jet rejection of 5 is
 1110 chosen (see Figure 4.9).

1111 The tagging efficiencies in Monte Carlo are corrected for b and c flavours with the ap-
 1112 propriate $\epsilon_{data}/\epsilon_{MC}$ scale factors, determined in bins of jet p_T and η .

1113 Tag Rate Function method

1114 When requiring ≥ 1 b -tagged jet the available Monte Carlo statistics is significantly re-
 1115 duced for some particular background processes, leading to large fluctuations in the resulting
 1116 distributions.

1117 To overcome this problem the Tag Rate Function (TRF) method is introduced. Here,
 1118 no event is rejected based on its b -tagging count, but instead all the events are kept and
 1119 weighted according to the probability of the given event to contain the desired number of
 1120 b -jets. The event weight is computed based on the kinematics and flavour of the jets found
 1121 in each event and using the tagging efficiency, which is a function of η , p_T and true jet

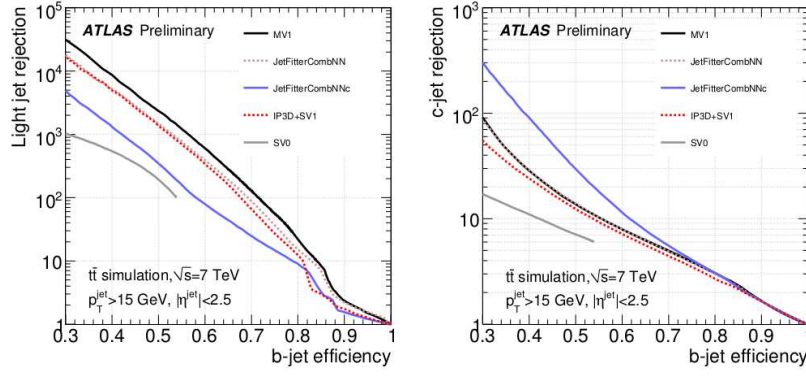


Figure 4.9: Light- (left) and c -jet (right) rejection as a function of the b -jet tagging efficiency for different tagging algorithms. These values refer to jets with $p_T > 15$ GeV and $|\eta| < 2.5$ in simulated $t\bar{t}$ events [59].

flavour.

Given a jet with η , p_T and flavour f , its tagging probability can be noted as:

$$\varepsilon(f, |\eta|, p_T)$$

For a given event with N jets, its probability of containing exactly one b -tag jet can be computed as:

$$P_{=1} = \sum_{i=1}^N \left(\varepsilon_i \prod_{j \neq i} (1 - \varepsilon_j) \right)$$

In the same way, it can be used to compute the probability for inclusive b -tag selections:

$$P_{=0} = \prod_{i=1}^N (1 - \varepsilon_i)$$

$$P_{\geq 1} = 1 - P_{=0}$$

Since this method relies on the correctness of the tagging efficiency, closure tests have been performed to check calibration of the tagging efficiency in Monte Carlo samples. These studies show that the efficiency parametrization officially provided [49] is not as accurate as expected, and therefore new efficiency maps were obtained. With correct calibrations the average of the histogram of $1/\varepsilon$ vs η , p_T and true jet flavour should be flat and with mean equal to one. Figure 4.10 shows these variables using the official and the new maps. It is clear that some regions of the light flavor map show high departure from closure, hence the new efficiency map will be used for the probability computations in the TRF method.

4.7 Missing Transverse Energy

To estimate the momentum of invisible particles in the event, i.e. neutrinos and, eventually, new particles, the missing transverse energy E_T^{miss} [60] is defined [49] to balance the

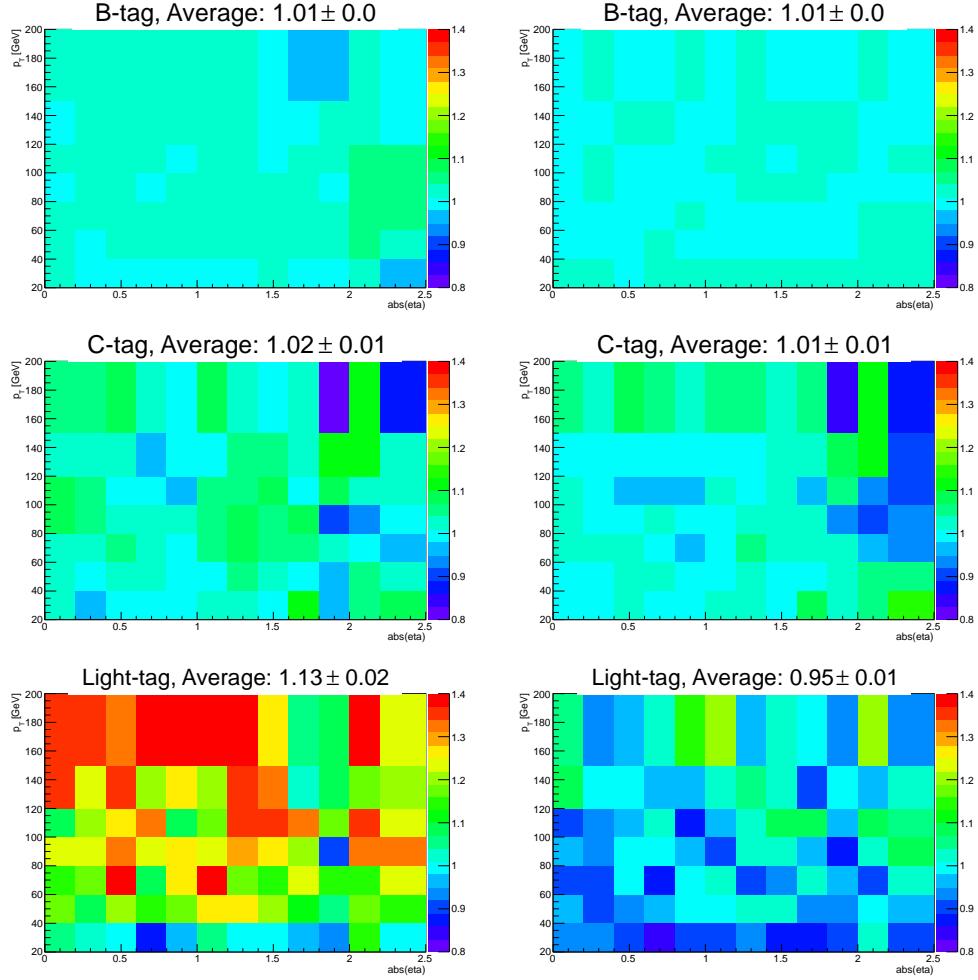


Figure 4.10: Results of the closure test using efficiency from the official calibration file (left column) and the private efficiency map (right column). The test is split in the different jet flavours: b jets (top), c jets (middle) and light jets (bottom).

total transverse momentum of the event. Indeed, while the longitudinal energy of the interacting partons is unknown, as they carry an unpredictable fraction of the total proton momentum, its transverse component is, initially, zero. Possible sources of fake contributions to the E_T^{miss} are detector coverage, dead or noisy regions and finite detector resolution.

The E_T^{miss} is computed by first matching each calorimeter energy deposit is with a high- p_T object, in the following order: electrons, photons, jets and muons. These are respectively the RefEle, RefGamma, RefJet, RefMuon terms, whether the low- p_T jets are grouped into the SoftJet term. Then, the energies of these objects are corrected accordingly to the respective calibration constants. The calorimeter clusters that did not get associated with any high- p_T object are calibrated for energy losses in dead material regions and for the different response to the electromagnetic and hadronic components of particle showers and added as the CellOut term. Finally the E_T^{miss} is computed as:

$$\begin{aligned} E_{x,y}^{\text{miss}} &= \frac{E_{x,y}^{\text{RefEle}} + E_{x,y}^{\text{RefGamma}} + E_{x,y}^{\text{RefJet}} + E_{x,y}^{\text{RefMuon}} + E_{x,y}^{\text{SoftJet}} + E_{x,y}^{\text{CellOut}}}{E_T^{\text{miss}}} \\ E_T^{\text{miss}} &= \sqrt{(E_x^{\text{miss}})^2 + (E_y^{\text{miss}})^2} \end{aligned} \quad (4.7)$$

1139 Searches for vector-like top partner 1140 pairs in the single lepton channel

1141

1142

1143 Starting from this chapter, and continuing in Chapter 6 and Chapter 7, we are going
1144 to describe two preliminary searches for vector-like top partners $T\bar{T}$ pairs performed in the
1145 single lepton¹ channel. These analyses are optimized for different final states and are thus
1146 complementary. The analyses are performed using a partial dataset of the p-p collisions
1147 at the center of mass energy of $\sqrt{s}=8$ TeV collected during 2012 at the ATLAS detector,
1148 consisting in 14.3 fb^{-1} . The first search focuses on vector-like top partners decay channels
1149 with high Branching Ratio (BR) to a W boson and a bottom quark, while the second search
1150 is optimized for events with high BR to a Higgs boson and a top quark.

1151 This chapter is devoted to the presentation of the general features that are common to the
1152 two analyses and is organized as follows: first in Section 5.1 we review the common strategy
1153 adopted in the ATLAS collaboration Exotics group for vector-like quark searches; Section 5.2
1154 summarises the common event preselection for data and few general concepts in the analyses
1155 design; Section 5.3.1 presents the Monte Carlo samples used in the searches, which are in
1156 general common to both analyses with only few exceptions that are reported; Section 5.3.2
1157 describes how the multi-jet background from QCD events is obtained; Section 5.4 introduces
1158 the general treatment of systematics. The two analyses are then presented in details in
1159 Chapter 6 ($T\bar{T}$ pairs decaying to $Wb+X$) and in Chapter 7 ($T\bar{T}$ pairs decaying to $Ht+X$).
1160 The final results are presented in Chapter 8.

1161 5.1 General strategy for vector-like quark pairs searches

1162 The phenomenology for vector-like quarks was described already in Section 1.2 of this
1163 dissertation, here we will only briefly re-introduce the concepts on which the strategy for

¹From now on, with the word “lepton” we will mean only either electron or muon, assumed to come from the leptonic decay of a W boson with its associated neutrino, which is considered to be the only particle contributing to the transverse missing energy E_T^{miss} .

the searches has been built. Table 5.1 collects the decay modes for vector-like quarks in the singlet and doublet models. It is evident from the richness of the final state phase space, combined with the unpredicted mass of the heavy objects that could span from few hundreds of GeVs (down to the values excluded by previous searches) up to order of one TeV (since we focus on pair production of vector-like quarks, which is favoured up to this mass scale as shown in Figure 5.1), that is impossible to cover it with a single inclusive search.

VLQ Singlets	Decay modes	VLQ Doublets	Decay modes
$T(+2/3)$	W^+b, Ht, Zt	$\begin{pmatrix} T \\ B \end{pmatrix}$	W^+b, Ht, Zt W^-t, Hb, Zb
$B(-1/3)$	W^-t, Hb, Zb	$\begin{pmatrix} T \\ X \end{pmatrix}$	Ht, Zt W^+t
$X(+5/3)$	W^+t	$\begin{pmatrix} B \\ Y \end{pmatrix}$	Hb, Zb W^-b
$Y(-4/3)$	W^-b		

Table 5.1: Allowed decay modes for vector-like singlets and doublets.

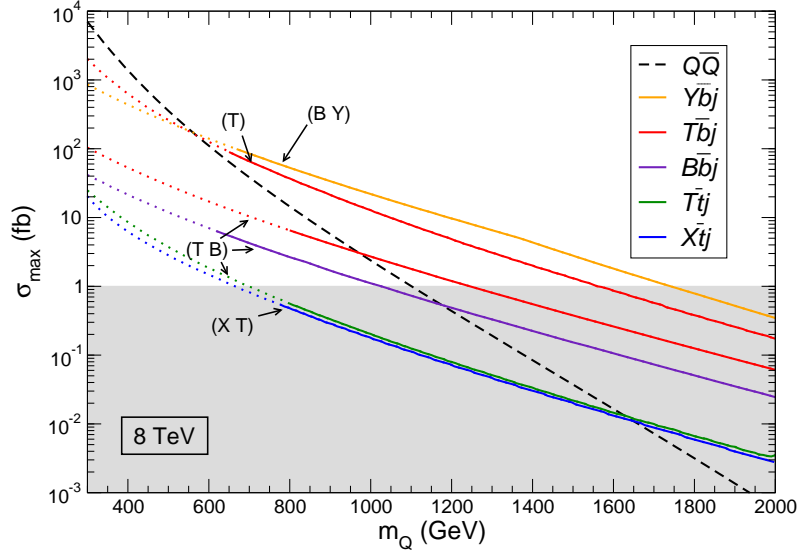


Figure 5.1: Pair and single production cross sections for heavy quarks in proton-proton collisions at $\sqrt{s} = 8$ TeV [61].

The BR of vector-like top and bottom partners to the allowed decay modes depends on the mass of the heavy quark and on the considered model (in our case, singlet or doublet scenario), as shown in Figure 5.2. Each decay mode has specific features that allow to define

powerful, optimized searches. Therefore in order to exploit this opportunity and at the same time stay as model independent as possible, different searches for vector-like quarks are performed at ATLAS to be later combined, each of them sensitive to specific channels. To ensure a comprehensive coverage of the phase space, a two-dimensional plane is defined (Figure 5.3) as follows: along the Y axes is the BR of the decay modes with a Higgs boson in the final state; along the X axis is the BR of the decay modes with a W boson in the final state. The BR to the channel with a Z boson in the final state is then fixed by the unitarity requirement $\text{BR}(T/B \rightarrow Zt/b) = 1 - \text{BR}(T/B \rightarrow Ht/b) - \text{BR}(T/B \rightarrow Wb/t)$. A plane of this kind is defined for every vector-like quark mass point considered in the analysis. Each point of each plane therefore represents a uniquely defined model, and analyses are performed for every configuration to either find deviations from expectations or to set a 95% Confidence Level (CL) exclusion. The final objective of the joint strategy is to cover the full plane.

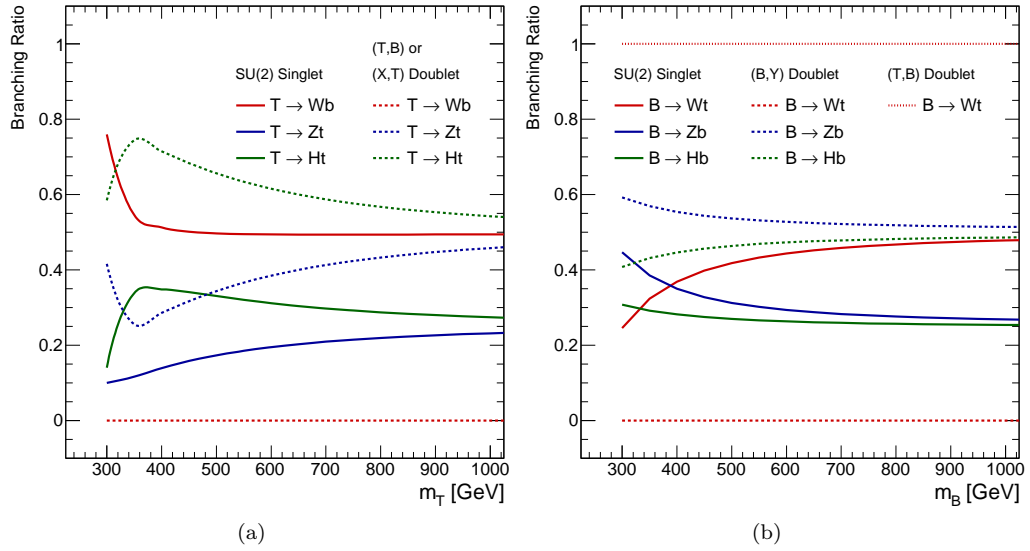


Figure 5.2: Branching ratio of vector-like top (a) and bottom (b) partners as a function of the heavy quark mass m_T and m_B respectively [62] for singlet and doublet models.

Up to the date of the writing of this dissertation, four complementary and quasi model-independent analyses have been performed by the Exotics working group on the partial dataset of 14.3 fb^{-1} of proton-proton collision data at $\sqrt{s} = 8 \text{ TeV}$. Two analyses investigated dilepton channels, one requiring a pair of same-charge leptons [63], the other a pair of opposite-charge leptons [62]. These two analyses are sensitive to both vector-like top and bottom partners, and the first in particular is also sensitive to four-top production $pp \rightarrow t\bar{t}t\bar{t}$, either through the Standard Model process or a beyond-SM source such as pair production of scalar color-octets (sgluons) or gluinos, with subsequent decays to top quark pairs. While the first search approach is to select via restrictive cuts the eventual signal and compare the final counts with the expected yields from background sources, the second search focuses on reconstructing the Z boson from the opposite-charge lepton pair and uses the invariant mass of the Z boson candidate paired with the highest p_T b -jet as final discriminant variable

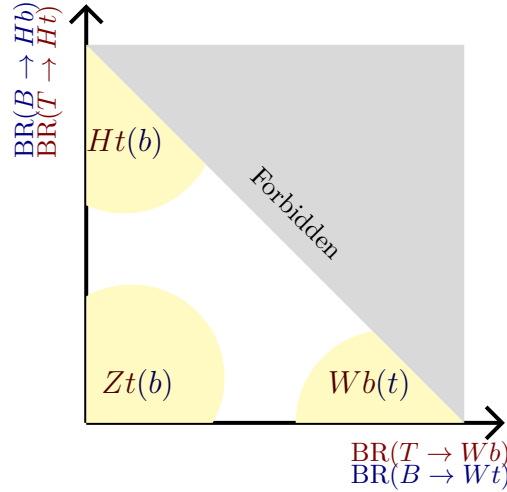


Figure 5.3: Two dimensional plane used to represent the comprehensive scan of model mixing. Searches with a Higgs boson in the final state cover the top left corner; searches with a Z boson in the final state cover the bottom left corner; searches with a W boson in the final state cover the bottom right corner. The shaded area labelled as “forbidden” is the unphysical region where $\text{BR}(T/B \rightarrow Ht/b) + \text{BR}(T/B \rightarrow Wb/t) + \text{BR}(T/B \rightarrow Zt/b) > 1$

1198 to perform the statistical analysis.

1199 We will in the following treat in details the two searches for vector-like top partners
 1200 performed in the single lepton channels, starting with the discussion of the common features
 1201 between the two analyses.

1202 5.2 Data sample and common event preselection

1203 The data from p-p collision events recorded at the ATLAS experiment during 2012 at
 1204 a center of mass energy of $\sqrt{s} = 8$ TeV are considered. Physics object definitions were
 1205 previously discussed in Chapter 4. Events collected during stable beam periods are required
 1206 to pass data quality requirements and single lepton trigger selection. In order to maximize
 1207 trigger efficiency, different transverse momentum threshold triggers are combined through a
 1208 logical OR, with the lower p_T ones including isolation requirements that result in inefficiencies
 1209 for high p_T lepton candidates, recovered with the use of the higher threshold triggers. The
 1210 electron triggers have p_T thresholds of 24 and 60 GeV, the muon ones of 24 and 36 GeV
 1211 (Section 4.4).

1212 After passing trigger requirements, events with more than one lepton are discarded. In
 1213 addition, the only lepton of the event has to match within $\Delta R < 0.15$ the triggered one. As
 1214 basic preselection, four jets satisfying the conditions described in Section 4.6 are required, at
 1215 least one of them being tagged as a b -jet.

1216 In order to suppress the multi-jet background from QCD processes, combined cuts on

	Wb	Ht	Zt
Wb	4 (2)	6 (4)	6 (2/4)
Ht	6 (4)	8 (6)	max: 8 (4/6) min: 6 (2)
Zt	6 (2/4)	max: 8 (4/6) min: 6 (2)	max: 8 (2/6) min: 6 (2/4)

Table 5.2: Jets (b -jets) multiplicities in the various possible final states. Z boson decays 55% hadronically, 15% of the times into $b\bar{b}$, therefore the min/max number of b -jets is reported. Highlighted in bold characters are the channels that after the orthogonality cut will contribute to the $T\bar{T} \rightarrow Wb + X$ analysis.

the E_T^{miss} and on the tranverse mass of the leptonically decaying W boson m_T^2 are defined: $E_T^{\text{miss}} > 20 \text{ GeV}$ and $E_T^{\text{miss}} + m_T > 60 \text{ GeV}$.

At this point, a simple consideration about the typical expected jet (and b -jet) multiplicity is made so as to define an orthogonality cut between the two analyses. Table 5.2 shows the number of jets (b -jets) per decay channel combinations of $T\bar{T}$ pairs, in the case of single lepton selection with at least four jets (i.e. one W boson will always decay into lepton and neutrino, and Z boson decay to neutrinos is excluded in the $WbZt$ channel) and assuming that the Higgs boson decays to a bottom quark-antiquark pair. To avoid overlap between selected events from the two analyses, in the $T\bar{T} \rightarrow Wb + X$ analysis events with ≥ 6 jets and ≥ 3 b -jets are rejected³.

5.3 Background and signal modeling

The main background for both analyses is $t\bar{t}$ production with jets ($t\bar{t}$ +jets in the following) and different choices for the generator are made in the analyses because of the specific needs of having well modeled regions. In the case of the $t\bar{t}$ +jets background prediction for the $T\bar{T} \rightarrow Ht + X$ analysis further corrections to match the data are applied, due to a mis-modeling in the heavy- and light-flavour content of the simulated sample (see Section 7.2).

W boson production in association with jets (W +jets in the following) and multi-jet events from QCD processed also contributes, the latter sneaking into the event selection via the misidentification of a jet or a photon as an electron or the presence of a non-prompt lepton from, e.g., semileptonic b - or c -hadron decay. Other background smaller components are single top quark, Z +jets, diboson (WW, WZ, ZZ), and $t\bar{t}$ production associated with a vector or Higgs boson.

All event generators using HERWIG [27] are also interfaced to JIMMY v4.31 [28] to simulate the underlying event. With the exception of the signal samples, all simulated samples utilise PHOTOS 2.15 [64] to model photon radiation and TAUOLA 1.20 [65] to model τ decays.

² $m_T = \sqrt{2p_T^\ell E_T^{\text{miss}}(1 - \cos \Delta\phi)}$, with p_T^ℓ being the transverse momentum (energy) of the muon (electron) and $\Delta\phi$ the azimuthal angle separation between the lepton and the direction of the missing transverse momentum.

³As will be explained later in Section 7.2, another orthogonality cut will be applied in the low b -jet multiplicity channel of the $T\bar{T} \rightarrow Ht + X$ analysis.

All simulated samples include multiple p-p interactions and go through the **GEANT4** [40] detector geometry and response simulation [39] with the exception of the signal samples, for which a fast simulation of the calorimeter response is used.

All simulated samples are then processed through the same reconstruction software as the data and are reweighted to match the instantaneous luminosity profile in data. For more details on the Monte Carlo simulation chain we refer the reader to Chapter 3 and in particular to Section 3.3.

5.3.1 Monte Carlo simulated samples

$t\bar{t}$ MC@NLO

Simulated samples of $t\bar{t}$ pair production in association with jets ($t\bar{t}$ +jets or simply $t\bar{t}$ in the following) are generated with **MC@NLO** v4.01 [66, 67, 68] using the **CT10** set of parton distribution functions (PDFs) [69], with the parton-shower and fragmentation steps being performed by **HERWIG** v6.520 [27]. The top quark mass is assumed to be equal to 172.5 GeV and the samples are normalized to approximate next-to-next-to-leading-order (NNLO) theoretical cross section [70]; the cross section used has been computed with **HATHOR** 1.2 [70] using the **MSTW2008** NNLO PDF set [17] and is $\sigma_{t\bar{t}} = 238^{+22}_{-24}$ pb, where the total uncertainty results from the sum in quadrature of the scale and PDF+ α_S uncertainties according to the **MSTW** prescription [71]. This is the $t\bar{t}$ used in the $T\bar{T} \rightarrow Wb + X$ analysis.

$t\bar{t}$ Alpgen

Simulated samples of $t\bar{t}$ +jets are generated using the **ALPGEN** v2.13 [29] leading-order (LO) generator and the **CTEQ6L1** PDF set [72], with parton shower and fragmentation modelled through **HERWIG** v6.520 [27].

A parton-jet matching scheme called “MLM matching” [73] is used in order to avoid double-counting of partonic configurations eventually generated both at the matrix-element calculation level and at the parton-shower evolution step.

Separate samples are generated for $t\bar{t}$ +light jets ($t\bar{t}$ +light or $t\bar{t}$ +LF in the following, from “light flavour”) with up to three additional light partons (u , d , s quarks or gluons), and for $t\bar{t}$ +heavy-flavour jets ($t\bar{t}$ +HF in the following), including $t\bar{t}b\bar{b}$ and $t\bar{t}c\bar{c}$. An algorithm based on the angular separation between the extra heavy quarks is used to remove the overlap between $t\bar{t}q\bar{q}$ ($q = b, c$) generated from the matrix element calculation and from parton-shower evolution in the $t\bar{t}$ +light samples is employed: matrix-element prediction is chosen over the parton-shower one when $\Delta R(q, \bar{q}) > 0.4$, else vice-versa.

Again a top quark mass of 172.5 GeV is assumed, and normalisation to the NNLO theoretical cross section is used (see 5.3.1)

W/Z +jets

Simulated samples of W/Z boson production in association with jets (W/Z +jets in the following) are generated with up to five additional partons using the **ALPGEN** v2.13 [29] LO generator and the **CTEQ6L1** PDF set [72], interfaced to **HERWIG** v6.520 for parton showering and fragmentation.

The MLM matching scheme is used also here to avoid double-counting of partonic configurations between matrix-element calculation and parton showering.

The W +jets samples are generated separately for W +light jets, $Wb\bar{b}$ +jets, $Wc\bar{c}$ +jets, and Wc +jets, with the relative contributions normalized using the fraction of b -tagged jets in W +1-jet and W +2-jets data control samples [74], while the Z +jets samples are generated separately for Z +light jets, $Zb\bar{b}$ +jets, and $Zc\bar{c}$ +jets and normalized to the inclusive NNLO theoretical cross section [75].

Overlap between $W/Zq\bar{q}$ +jets ($q = b, c$) events generated from the matrix element calculation and those generated from parton-shower evolution in the W/Z +light jets samples is avoided via an algorithm analogous to the one used for $t\bar{t}$ Alpgen.

For the W +jets background, a normalisation from data for the shapes obtained from the simulation is derived since the simulation overestimates the number of W +jets events by up to $\sim 20\%$, depending on the jet multiplicity.

By exploiting the predicted asymmetry between W^+ +jets and W^- +jets production in p-p collisions [76], the total number of W +jets events in data ($N_W = N_{W^+} + N_{W^-}$), can be estimated based on the measured difference between the number of positively- and negatively-charged W bosons, $(N_{W^+} - N_{W^-})_{\text{meas}}$, and the asymmetry predicted from the simulation:

$$N_W = \left(\frac{N_{W^+} + N_{W^-}}{N_{W^+} - N_{W^-}} \right)_{\text{MC}} (N_{W^+} - N_{W^-})_{\text{meas}} \quad (5.1)$$

Events are categorised in terms of multiplicity of b and c jets and scale factors are derived using Equation 5.1. The fraction of W +light jets events is scaled accordingly in order to preserve the overall normalisation of the W +jets background before b tagging.

Other backgrounds

Simulated samples of single top quark backgrounds corresponding to the s -channel and Wt production mechanisms are generated with MC@NLO v4.01 [66, 67, 68] using the CT10 PDF set [69]. In the case of t -channel single top quark production, the ACERMC v3.8 LO generator [38] with the MRST LO** PDF set is used.

Simulated samples of $t\bar{t}$ produced in association with a W or Z boson ($t\bar{t}V$ ($V = W, Z$) in the following) are generated with the MADGRAPH v5 LO generator [37] and the CTEQ6L1 PDF set.

Samples of $t\bar{t}$ produced in association with a Higgs boson ($t\bar{t}H$ in the following) are generated with the PYTHIA 6.425 [77] LO generator and the MRST LO** PDF set [78], assuming a Higgs boson mass of 125 GeV and considering the $H \rightarrow b\bar{b}$, $c\bar{c}$, gg , and W^+W^- decay modes.

Parton shower and fragmentation are modelled with HERWIG v6.520 [27] in the case of MC@NLO, with PYTHIA 6.421 in the case of ACERMC, and with PYTHIA 6.425 in the case of MADGRAPH. All these samples are generated assuming a top quark mass of 172.5 GeV. The single top quark samples are normalised to the approximate NNLO theoretical cross sections [79, 80] using the MSTW2008 NNLO PDF set, while the $t\bar{t}V$ samples are normalised to the NLO cross section predictions [81, 82]. The $t\bar{t}H$ sample is normalised using the NLO theoretical cross section and branching ratio predictions [83]. Finally, the diboson

backgrounds are modelled using **HERWIG** with the **MRST L0**** PDF set, and are normalised to their NLO theoretical cross sections [84].

Signal samples

For vector-like T signals, samples corresponding to a singlet T quark decaying to Wb , Zt and Ht are generated with the **PROTOS v2.2** LO generator [85, 86] using the **MSTW2008** LO PDF set, and interfaced to **PYTHIA** for the parton shower and fragmentation.

For each decay channel (Wb , Zt and Ht) the branching ratio has been set to $1/3$. Events are reweighted in order to reproduce any desired branching ratio configuration.

The predicted branching ratios in the weak-isospin singlet and doublet scenarios as a function of m_T are given in Table 5.3.

The m_T values considered range from 350 GeV to 850 GeV in steps of 50 GeV, with the Higgs boson mass assumed to be 125 GeV. All Higgs boson decay modes are considered, with branching ratios as predicted by **hdecay** [87].

Signal samples are normalized to the approximate NNLO theoretical cross sections [70] using the **MSTW2008** NNLO PDF set. The cross section values used are summarized in Table 5.4.

m_T (GeV)	$BR(T \rightarrow Wb)$	Singlet		$BR(T \rightarrow Wb)$	Doublet	
		$BR(T \rightarrow Zt)$	$BR(T \rightarrow Ht)$		$BR(T \rightarrow Zt)$	$BR(T \rightarrow Ht)$
350	0.545	0.116	0.338	0.000	0.255	0.745
400	0.513	0.139	0.348	0.000	0.285	0.715
450	0.502	0.158	0.341	0.000	0.316	0.684
500	0.497	0.173	0.330	0.000	0.343	0.657
550	0.495	0.185	0.321	0.000	0.365	0.635
600	0.494	0.194	0.312	0.000	0.383	0.617
650	0.494	0.202	0.304	0.000	0.399	0.601
700	0.494	0.208	0.298	0.000	0.411	0.589
750	0.494	0.214	0.292	0.000	0.422	0.578
800	0.494	0.218	0.288	0.000	0.431	0.569
850	0.494	0.222	0.284	0.000	0.439	0.561

Table 5.3: Branching ratios for T decay as a function of m_T as computed with **PROTOS** in the weak-isospin singlet and doublet scenarios. The same values are used in the graphical representation of Figure 5.2

5.3.2 Multi-jet background

QCD production can pass the event selection in the electron channel as non-prompt electrons or as “fake” electrons, i.e. either electrons from photon conversions or mis-identified jets that left a high amount of energy in the electromagnetic calorimeter. For events in the muon channel the main contributions come from non-prompt leptons from semileptonic b - and c -hadron decays.

Even though these kind of events rarely pass the quality cuts required at the lepton reconstruction stage, the production cross section is so high (orders of magnitude more than $t\bar{t}$ pair production) that the contribution to the background from multi-jet events is no more negligible. The rate of what we will call in the following “fake events” (against “real

m_T (GeV)	$\sigma(TT)$ (pb)	Scale uncertainties (pb)	PDF+ α_s uncertainties (pb)	Total uncertainty (pb)
350	5.083	+0.140/-0.285	+ 0.569/-0.488	+0.586/-0.565
400	2.296	+0.066/-0.130	+ 0.269/-0.221	+0.277/-0.257
450	1.113	+0.034/-0.063	+ 0.136/-0.107	+0.140/-0.125
500	0.5702	+0.0185/-0.0327	+ 0.0723/-0.0545	+0.0746/-0.0636
550	0.30545	+0.01040/-0.01769	+ 0.04012/-0.02889	+0.0414/-0.0339
600	0.1696	+0.0060/-0.0099	+ 0.0230/-0.0161	+0.0238/-0.0189
650	0.09707	+0.00359/-0.00571	+ 0.01363/-0.00936	+0.01410/-0.01097
700	0.05694	+0.00218/-0.00338	+ 0.00828/-0.00559	+0.00856/-0.00653
750	0.03411	+0.00135/-0.00204	+ 0.00513/-0.00343	+0.00530/-0.00400
800	0.02080	+0.00085/-0.00126	+ 0.00329/-0.00216	+0.00340/-0.00250
850	0.01287	+0.00054/-0.00079	+ 0.00215/-0.00138	+0.00222/-0.00159

Table 5.4: Theoretical cross section at NNLO for TT production as a function of m_T as computed by HATHOR, and scale and PDF uncertainties. The same values are used in the graphical representation of Figure 5.1.

events”) is estimated via data-driven methods, since simulation is not expected to predict this contribution with the desired level of accuracy.

The technique used is called “Matrix Method” (MM in the following) [88]. The basic principle is to divide the data sample into two categories, one of events passing our standard selection criteria (“tight” events), the other including also leptons satisfying looser requirements (“loose” events). We can reasonably think that loose leptons are either real leptons or fake leptons, and that most of our real leptons will pass the tight selection. We consider then a good evaluation of multi-jet contamination that fraction of fake events going through the tight requirements. A pictorial representation of the sampling space is shown in Figure 5.4(a).

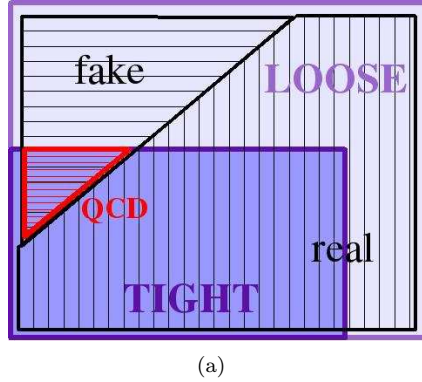


Figure 5.4: The events passing loose selection criteria can be real or fake leptons. Tighter requirements are added to the loose selection ones to define a sample of tight event which will contain real leptons as well as multi-jet background events.

Defining $N_{\text{real}}^{\text{loose}}$ ($N_{\text{fake}}^{\text{loose}}$) as the number of real (fake) leptons events satisfying the loose selection requirements, and $N_{\text{real}}^{\text{tight}}$ ($N_{\text{fake}}^{\text{tight}}$) as the number of real (fake) leptons events satisfying the tight selection requirements, we can write:

$$N^{\text{loose}} = N_{\text{real}}^{\text{loose}} + N_{\text{fake}}^{\text{loose}}, \quad (5.2)$$

$$N^{\text{tight}} = \epsilon_{\text{real}} N_{\text{real}}^{\text{loose}} + \epsilon_{\text{fake}} N_{\text{fake}}^{\text{loose}}. \quad (5.3)$$

1355 where ϵ_{real} (ϵ_{fake}) is the *efficiency* of selecting real (fake) loose leptons as tight leptons, i.e.:

$$\epsilon_{\text{real}} = \frac{N_{\text{real}}^{\text{tight}}}{N_{\text{real}}^{\text{loose}}}, \quad (5.4)$$

$$\epsilon_{\text{fake}} = \frac{N_{\text{fake}}^{\text{tight}}}{N_{\text{fake}}^{\text{loose}}}. \quad (5.5)$$

1356 The number we are interested in to estimate the background from multi-jet events is
 1357 the amount of fake leptons leaking into the tight selection region, which comes out from
 1358 elaborating the previous equations and is:

$$N_{\text{fake}}^{\text{tight}} = \frac{\epsilon_{\text{fake}}}{\epsilon_{\text{real}} - \epsilon_{\text{fake}}} (N_{\text{real}}^{\text{loose}} \epsilon_{\text{real}} - N^{\text{tight}}). \quad (5.6)$$

1359 An important condition for this method to work is that $\epsilon_{\text{real}} \gg \epsilon_{\text{fake}}$, which holds as
 1360 $\epsilon_{\text{real}} \sim 1$, while ϵ_{fake} is in general well below 1. ϵ_{real} is in general measured from tag and
 1361 probe measurements on Z boson decays to two leptons, while ϵ_{fake} is measured in control
 1362 regions enriched in multi-jet event contributions.

1363 In Appendix A the MM used for the estimation of multi-jet background in the muon
 1364 single lepton channel is described in some more details, as the author of this dissertation
 1365 directly contributed to its development.

1366 5.4 Systematical uncertainties treatment

1368 **Preliminary search for $T\bar{T}$ pairs**
1369 **decaying to $Wb + X$**

1370

1371 **6.1 Boosted W reconstruction**

1372 **6.2 Control regions**

1373 **6.3 Event selection**

1374 **6.4 Systematics**

1376 Preliminary search for $T\bar{T}$ pairs
1377 decaying to $Ht + X$

1378

1379 7.1 Control regions

1380 7.2 Event selection

1381 7.3 Systematics

Results

1383

1384

8.1 Combination

1385

1386 Conclusions

1387

Multi-jet background estimation in the single muon plus jets channel

1391

We report in this appendix the method developed in 2011 to better predict the contribution from multi-jet background events in analyses with a single muon and jets in the final state. We refer to Section 5.3.2 for the description of the general approach of the Matrix Method and will present here the improvements we made in the estimation by introducing a parametrization of the ϵ_{fake} as a function of the lepton transverse momentum and of the minimum of $\Delta R(\mu, j)$.

These parametrizations for the fake efficiencies are combined with the already consolidated parametrization in terms of muon pseudorapidity, which was used before.

The idea is that an increase in leading jet p_T corresponds to higher hadronic activity nearby the lepton, which results in the fact that the event will no longer satisfy the tight selection requirement of isolation $\min \Delta R(\mu, j) > 0.4$. This means a lower ϵ_{fake} . For the same reason we expect the fake efficiency to be lower for muons closer to jets. We also expect this effects to increase with the number of jets in the event, a dependence that should be entering in the ϵ_{fake} parametrization as a function of $\min \Delta R(\mu, j)$ (see Figure A.1 and A.2).

The muons are selected as “tight” if they pass the standard selection described in Section??, while for the “loose” selections the requirements on calorimeter and tracker isolation ($etcone30 < 4$ GeV and $ptcone30 < 4$ GeV respectively) are dropped.

cut	loose	tight
track ID quality cuts	✓	✓
combined muon	✓	✓
tight muon	✓	✓
$\min \Delta R(\mu, j) > 0.4$	✓	✓
e/μ overlap removal	✓	✓
etcone30Isolation		✓
ptcone30Isolation		✓

Table A.1

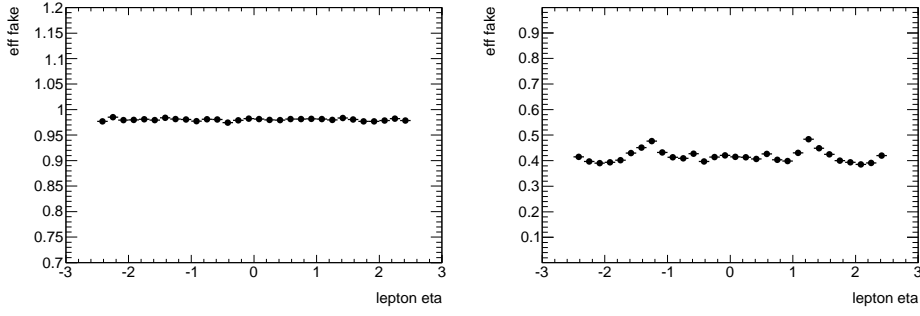


Figure A.1: Lepton η dependency of ϵ_r (left plot) and ϵ_f (right plot).

	ϵ_f	ϵ_r
untagged	0.4178 ± 0.0006	0.9805 ± 0.0003
tagged	0.353 ± 0.002	0.973 ± 0.006

Table A.2: Average values for ϵ_f and ϵ_r in untagged and tagged channels. Error is only statistical.

1409 ϵ_{real} is estimated in a sample of $Z \rightarrow \mu\mu$ restricted to events with exactly 2 muons, one
 1410 “tight” and one “loose” and requiring the dilepton reconstructed mass of the boson to be
 1411 between 80-100 GeV. The control region to estimate ϵ_f is chosen as $5 \text{ GeV} < E_T^{\text{Miss}} < 15 \text{ GeV}$
 1412 in order to isolate a sample enriched in QCD, then the event is required to have a “loose”
 1413 muon and at least one jet. Since contamination from muons from W and Z decays is still
 1414 present in the low E_T^{Miss} region, we try to achieve higher purity by correcting N^{tight} and
 1415 N^{loose} as

$$N_{\text{corr}}^{\text{tight}} = N^{\text{tight}} - N_{W+\text{jets},MC}^{\text{tight}} - N_{Z+\text{jets},MC}^{\text{tight}} - N_{t\bar{t},MC}^{\text{tight}} \quad (\text{A.1})$$

$$N_{\text{corr}}^{\text{loose}} = N^{\text{loose}} - N_{W+\text{jets},MC}^{\text{loose}} - N_{Z+\text{jets},MC}^{\text{loose}} - N_{t\bar{t},MC}^{\text{loose}} \quad (\text{A.2})$$

Figure A.1 and A.2 show ϵ_r as a function of muon η and ϵ_f as a function of the variables on which we parametrize, i.e. muon η , leading jet p_T and the minimum of $\Delta R(\mu, j)$. The functions used don’t have a specific physical meaning and are respectively

$$f_{LJpT}(x) = p_0 + p_1/(x/100)^{p_2} \quad (\text{A.3})$$

and

$$f_{\min\Delta R}(x) = 0.5p_0(1 + T\text{Math} :: \text{Erf}((x - p_1)/(\sqrt{2}p_2))). \quad (\text{A.4})$$

1416 If we add the requirement of having at least one tagged jet in the event, the efficiencies
 1417 change (see Table A.2). Efficiencies are computed in the same way as the untagged case
 1418 (see Appendix ?? for more details) but in the end the untagged ϵ_r is used also for the
 1419 tagged events since no significant variation is observed and we have more statistics for the
 1420 estimation.

These two dependencies are then combined together to obtain a weight for the value of

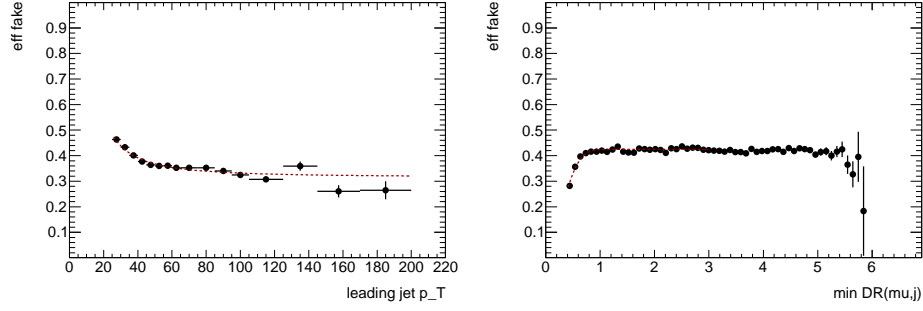


Figure A.2: Parametrization of ϵ_f as a function of the leading jet p_T (left plot) and of the minimum ΔR between muon and jets (right plot).

	= 1 jet	= 2 jets	= 3 jets	≥ 4 jets
$t\bar{t}$	304.33 ± 7.41	1320.55 ± 15.50	2709.63 ± 22.13	4702.33 ± 29.49
QCD	24803.36 ± 153.57	10511.66 ± 87.94	2942.08 ± 43.72	1049.85 ± 25.02
W+jets	385242.06 ± 1129.55	98826.98 ± 373.93	23614.51 ± 154.62	7419.73 ± 81.07
Z+jets	17257.90 ± 63.81	5478.57 ± 35.64	1553.30 ± 18.79	592.78 ± 11.28
Single top	1002.70 ± 10.77	1126.85 ± 10.55	578.51 ± 6.47	285.44 ± 4.15
Total prediction	428610.34 ± 1141.80	117264.61 ± 386.23	31398.04 ± 163.41	14050.14 ± 90.62
Data	437526	112984	29135	12779

Table A.3: Yields table for the data and background samples for different jet multiplicities in the untagged full event selection.

the fake efficiency at a given η :

$$\epsilon_f = \epsilon_f(\eta) \frac{f_{\min \Delta R}(\min \Delta R)}{\langle \epsilon_f^{\min \Delta R} \rangle} \frac{f_{LJpT}(LJpT)}{\langle \epsilon_f^{LJpT} \rangle} \quad (\text{A.5})$$

Figure A.3 shows the agreement between data and MonteCarlo backgrounds when also the QCD estimated with this Matrix Method is considered. Here the events satisfy the full selection with exactly 1 jet before and after applying the triangular cut $E_T^{Miss} + m_T(W) > 60$ GeV, and no btagging information is required. Adding the tagging selection leads to the comparison plots of Figure A.4 where the full selection (with and without the triangular cut) leave exactly 2 jets of which at least one has been tagged as a bjet. The variables $p_T(\mu)$, E_T^{Miss} and $m_T(W)$ are chosen to illustrate the QCD prediction since it is known that here the QCD will peak at low values. In the Appendix ?? more plots for other jet multiplicities can be found.

The two plots in Figure A.5 show the total amount of events for data and backgrounds in the untagged and tagged channels in different jet multiplicity bins. The numerical values for the QCD estimate are reported in Table A.3 and Table A.4 for the untagged and tagged case respectively.

An estimation of the systematic uncertainties on the QCD can be derived considering the following sources:

1. statistical error on ϵ_f and ϵ_r ;

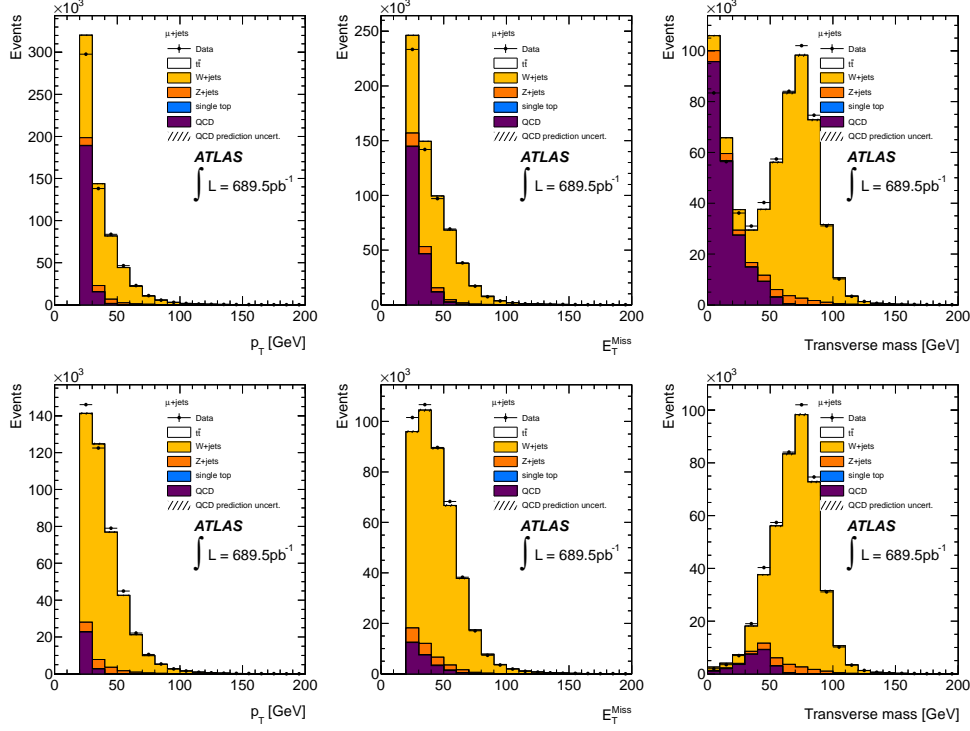


Figure A.3: Comparison plots between data and backgrounds (MonteCarlo and QCD) for the muon transverse momentum (left column), missing transverse energy (central column) and the transverse mass of the W (right column). The full event selection of 1 jet exclusive with no btagging information is used without and with the triangular cut (top and bottom respectively).

	= 1 jet	= 2 jets	= 3 jets	≥ 4 jets
$t\bar{t}$	108.35 ± 4.22	689.18 ± 10.58	1659.28 ± 16.48	3185.88 ± 23.19
QCD	1449.22 ± 29.45	1109.84 ± 24.17	420.08 ± 14.44	211.11 ± 10.35
W+jets	4392.92 ± 77.83	3016.70 ± 56.17	1280.12 ± 38.41	612.50 ± 26.04
Z+jets	104.68 ± 4.76	94.69 ± 4.56	52.10 ± 3.32	28.77 ± 2.44
Single top	359.78 ± 6.16	522.23 ± 6.80	307.53 ± 4.50	159.42 ± 2.96
Total prediction	6414.95 ± 83.69	5432.64 ± 62.60	3719.11 ± 44.57	4197.68 ± 36.58
Data	7243	5634	3876	4406

Table A.4: Yields table for the data and background samples for different jet multiplicities in the tagged full event selection (at least one bjet).

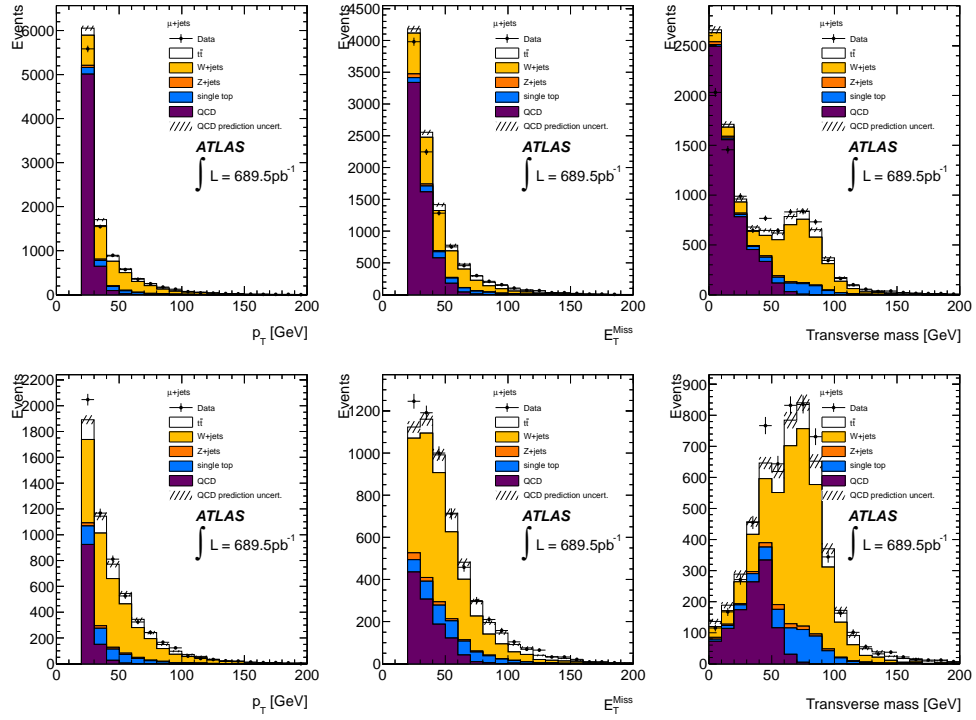


Figure A.4: Comparison plots between data and backgrounds (MonteCarlo and QCD) for the muon transverse momentum (left column), missing transverse energy (central column) and the transverse mass of the W (right column). The full event selection of 2 jet exclusive with at least 1 btagged jet is used without and with the triangular cut (top and bottom respectively).

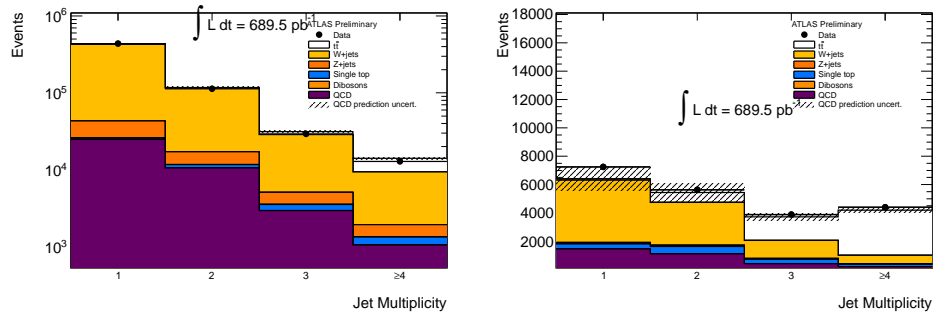


Figure A.5: Yields plots for data and backgrounds requiring full event selection (left plot) and full event selection plus at least one btagged jet (right plot) in jet multiplicity bins.

	= 1 jet	= 2 jets	= 3 jets	≥ 4 jets
ε_1	0.1%			
ε_2	0.6%	0.8%	1.5%	2.4%
ε_3	7.9%	21.2%	31.0%	41.3%

Table A.5: Systematic uncertainties on QCD estimation for different jet multiplicity in the untagged case.

	= 1 jet	= 2 jets	= 3 jets	≥ 4 jets
ε_1	0.5%			
ε_2	2.0%	2.2%	3.4%	4.9%
ε_3	6.4%	18.5%	26.5%	32.4%

Table A.6: Systematic uncertainties on QCD estimation for different jet multiplicity in the tagged case.

- 1437 2. statistical error on the QCD estimation;
- 1438 3. different control regions for the estimation of fake efficiency;
- 1439 4. changes in the parametrization used.

1440 For the points 1 and 2, the values can be taken from what already shown in Table A.2 and
 1441 Table A.3 and A.4. For what concerns point 3, we compared the results obtained in control
 1442 region $5 \text{ GeV} < E_T^{Miss} < 15 \text{ GeV}$ with an estimation in control region $E_T^{Miss} < 10 \text{ GeV}$,
 1443 while no studies have yet been performed about point 4. Table A.5 and A.6 summarize the
 1444 systematic uncertainties for different jet multiplicity in the untagged and tagged channels
 1445 respectively.

Search for $T\bar{T} \rightarrow Wb + X$ at $\sqrt{7}$ TeV

Bibliography

-
- [1] ATLAS Collaboration, *The ATLAS Experiment at the CERN Large Hadron Collider*, **JINST** **3** (2008) S08003.
- [2] J. Aguilar-Saavedra, *Identifying top partners at LHC*, **JHEP** **0911** (2009) 030, [arXiv:0907.3155 \[hep-ph\]](#).
- [3] S. P. Martin, *Extra vector-like matter and the lightest Higgs scalar boson mass in low-energy supersymmetry*, **Phys.Rev.** **D81** (2010) 035004, [arXiv:0910.2732 \[hep-ph\]](#).
- [4] D0 Collaboration Collaboration, S. Abachi and et al., *Search for High Mass Top Quark Production in $p\bar{p}$ Collisions at $\sqrt{s} = 1.8$ TeV*, **Phys. Rev. Lett.** **74** (Mar 1995) 2422, <http://link.aps.org/doi/10.1103/PhysRevLett.74.2422>.
- [5] CDF Collaboration Collaboration, F. Abe and et al., *Observation of Top Quark Production in $p\bar{p}$ Collisions with the Collider Detector at Fermilab*, **Phys. Rev. Lett.** **74** (1995) 2626, <http://link.aps.org/doi/10.1103/PhysRevLett.74.2626>.
- [6] ATLAS Collaboration, *Observation of a new particle in the search for the Standard Model Higgs boson with the ATLAS detector at the LHC*, **Phys.Lett.** **B716** (2012) 1–29, [arXiv:1207.7214 \[hep-ex\]](#).
- [7] CMS Collaboration, *The CMS experiment at the CERN LHC*, **JINST** **3** (2008) S08004.
- [8] ALICE Collaboration, *The ALICE experiment at the CERN LHC*, **JINST** **3** (2008) S08002.
- [9] LHCb Collaboration, *The LCHb experiment at the CERN LHC*, **JINST** **3** (2008) S08005.
- [10] L. Evans, P. Bryant (Eds.), *LHC Machine*, **JINST** **3** (2008) S08001.

- [11] M. Lamont, *The First Years of LHC Operation for Luminosity Production*, in *Proceedings of 4th International Particle Accelerator Conference (IPAC 2013)* (2013) .
- [12] ATLAS Collaboration, *Luminosity determination in pp collisions at $\sqrt{s} = 7$ TeV using the ATLAS detector at the LHC*, *Eur. Phys. J. C* **71** (2011) 1630, [arXiv:1101.2185 \[hep-ex\]](#).
- [13] ATLAS Collaboration, *Studies of the performance of the ATLAS detector using cosmic-ray muons*, *Eur. Phys. J. C* **71** (2011) 1593.
- [14] W. R., *Calorimetry*, *Scientifica Acta* **2** (1) (2008) 1855.
- [15] ATLAS Collaboration, *Readiness of the ATLAS liquid argon calorimeter for LHC collisions*, *Eur. Phys. J. C* **70** (2010) 723–753.
- [16] ATLAS Collaboration, *Readiness of the ATLAS Tile calorimeter for LHC collisions*, *Eur. Phys. J. C* **70** (2010) 11931236.
- [17] A. Martin, W. Stirling, R. Thorne, and G. Watt, *Parton distributions for the LHC*, *Eur.Phys.J. C* **63** (2009) 189–285, [arXiv:0901.0002 \[hep-ph\]](#).
- [18] R. P. Feynman, *Very high-energy collisions of hadrons*, *Phys.Rev.Lett.* **23** (1969) 1415–1417.
- [19] J. M. Campbell, J. Huston, and W. Stirling, *Hard Interactions of Quarks and Gluons: A Primer for LHC Physics*, *Rept.Prog.Phys.* **70** (2007) 89, [hep-ph/0611148](#).
- [20] M. L. Mangano and T. J. Stelzer, *Tools for the simulation of hard hadronic collisions*, *Annu. Rev. Nucl. Part. Sci.* **55** (2005) no. CERN-PH-TH-2005-074, 555–588.
- [21] S. Gieseke, *Parton Shower Monte Carlos*, .
<http://th-workshop2009.desy.de/e59393/e59379/infoboxContent59381/Gieseke.pdf>.
- [22] F. Ambroglini, R. Armillis, P. Azzi, G. Bagliesi, A. Ballestrero, et al., *Proceedings of the Workshop on Monte Carlo’s, Physics and Simulations at the LHC. Part I*, [arXiv:0902.0293 \[hep-ph\]](#).
- [23] S. Catani, F. Krauss, R. Kuhn, and B. Webber, *QCD matrix elements + parton showers*, *JHEP* **0111** (2001) 063, [arXiv:hep-ph/0109231 \[hep-ph\]](#).
- [24] M. L. Mangano, M. Moretti, F. Piccinini, and M. Treccani, *Matching matrix elements and shower evolution for top-quark production in hadronic collisions*, *JHEP* **0701** (2007) 013, [arXiv:hep-ph/0611129 \[hep-ph\]](#).
- [25] S. Catani, Y. Dokshitzer, M. Olsson, G. Turnock, and B. Webber, *New clustering algorithm for multijet cross sections in $e+e$ annihilation*, *Physics Letters B* **269** (1991) no. 34, 432 – 438.
<http://www.sciencedirect.com/science/article/pii/037026939190196W>.
- [26] S. M. T. Sjostrand and P. Skands, *PYTHIA 6.4 physics and manual*, *JHEP* **05** (2006) 026, [arXiv:hep-ph/0603175](#).

- [27] G. Corcella *et al.*, *HERWIG 6: An event generator for hadron emission reactions with interfering gluons (including supersymmetric processes)*, JHEP **01** (2001) 010, [arXiv:hep-ph/0011363](#).
- [28] J. Butterworth, J. Forshaw, and M. Seymour, *Multiparton interactions in photoproduction at HERA*, Z. Phys. C **72** (1996) 637, [arXiv:9601371 \[hep-ph\]](#).
- [29] M. Mangano *et al.*, *ALPGEN, a generator for hard multiparton processes in hadronic collisions*, JHEP **07** (2003) 001, [arXiv:hep-ph/0206293](#).
- [30] F. Caravaglios, M.L. Mangano, M. Moretti and R. Pittau, *A New Approach to Multi-jet Calculations in Hadron Collisions*, Nucl. Phys. B **539** (1999) 215, [arXiv:hep-ph/9807570](#).
- [31] J. Campbell, R. K. Ellis, and D. Rainwater, *Next-to-leading order QCD predictions for $W + 2$ jet and $Z + 2$ jet production at the CERN LHC*, Phys. Rev. D **68** (2003) 094021.
- [32] R. Gavin, Y. Li, F. Petriello, and S. Quackenbush, *FEWZ 2.0: A code for hadronic Z production at next-to- next-to-leading order*, [arXiv:1011.3540 \[hep-ph\]](#).
- [33] S. Frixione and B. Webber, *The MC@NLO 3.2 event generator*, [arXiv:hep-ph/0601192](#).
- [34] F. K. M. S. S. S. e. a. T. Gleisberg, S. Hoeche, *Event generation with SHERPA 1.1*, JHEP **007** (2009) 0902, [arXiv:0811.4622 \[hep-ex\]](#).
- [35] P. N. Keith Hamilton, *Improving NLO-parton shower matched simulations with higher order matrix elements*, [arXiv:1004.1764 \[hep-ex\]](#).
- [36] P. Nason, *A new method for combining NLO QCD with shower Monte Carlo algorithms*, JHEP **11** (2004) 040.
- [37] J. Alwall *et al.*, *MadGraph/MadEvent v4: the new web generation*, JHEP **09** (2007) 028, [arXiv:0706.2334 \[hep-ph\]](#).
- [38] B. P. Kersevan and E. Richter-Was, *The Monte Carlo Event Generator AcerMC 2.0 with Interfaces to PYTHIA 6.2 and HERWIG 6.5*, [arXiv:0405247 \[hep-ph\]](#).
- [39] ATLAS Collaboration, *The ATLAS Simulation Infrastructure*, Eur.Phys.J. **70** (2010) 823, [arXiv:1005.4568 \[physics.ins-det\]](#).
- [40] S. Agostinelli *et al.*, *Geant4: a simulation toolkit*, Nucl. Instr. Meth. A **506** (2003) 250.
- [41] ATLAS Collaboration, *Expected Performance of the ATLAS Experiment - Detector, Trigger and Physics*, [arXiv:0901.0512 \[hep-ex\]](#).
- [42] T. Cornelissen, M. Elsing, S. Fleischmann, W. Liebig, E. Moyse, and A. Salzburger, *Concepts, Design and Implementation of the ATLAS New Tracking (NEWT)*, Tech. Rep. ATL-SOFT-PUB-2007-007. ATL-COM-SOFT-2007-002, CERN, Geneva, Mar, 2007.

- [43] R. Frhwirth, *Application of Kalman filtering to track and vertex fitting*,
Nuclear Instruments and Methods in Physics Research **262** (1987) no. 23, 444 – 450.
<http://www.sciencedirect.com/science/article/pii/0168900287908874>.
- [44] ATLAS Collaboration Collaboration, *Performance of primary vertex reconstruction in proton-proton collisions at $\sqrt{s}=7$ TeV in the ATLAS experiment*, Tech. Rep. ATLAS-CONF-2010-069, CERN, Geneva, Jul, 2010.
- [45] ATLAS Collaboration Collaboration, *Performance of the ATLAS Inner Detector Track and Vertex Reconstruction in the High Pile-Up LHC Environment*, Tech. Rep. ATLAS-CONF-2012-042, CERN, Geneva, Mar, 2012.
- [46] W. Lampl et al., *Calorimeter clustering algorithms: Description and performance*, ATL-LARG-PUB-2008-002 (2012) . <https://cdsweb.cern.ch/record/1099735>.
- [47] ATLAS Collaboration, *Electron performance measurements with the ATLAS detector using the 2010 LHC proton-proton collision data*, Eur.Phys.J. **C72** (2012) 1909, [arXiv:1110.3174 \[hep-ex\]](https://arxiv.org/abs/1110.3174).
- [48] E. Abat, J. Abdallah, T. Addy, P. Adragna, M. Aharrouche, et al., *Combined performance studies for electrons at the 2004 ATLAS combined test-beam*, JINST **5** (2010) P11006.
- [49] B. Acharya, J. Adelman, S. Adomeit, M. Aoki, B. Alvarez, F. Balli, W. Bell, K. Becker, K. Behr, D. Benjamin, E. Bergeas Kuutmann, C. Bernard, K. Black, S. Calvet, R. Camacho, Y. Coadou, G. Cortiana, N. Cooper-Smith, T. Cornelissen, M. Cristinziani, V. Dao, U. De Sanctis, C. Doglioni, F. Derue, K. Finelli, K. Grahn, J. Groth-Jensen, S. Head, A. Henrichs, D. Hirschebuehl, V. Kaushik, O. Kind, H. Khandanyan, A. Krasznahorkay, T. Kuhl, E. Le Menedeu, H. Lee, A. Lister, K. Loureiro, L. Miljovic, J. Morris, R. Moles Valls, O. Nackenhorst, D. Pelikan, M. Owen, M. Pinamonti, K. Rao, K. Rosbach, M. Rudolph, G. Salamanna, J. Schwindling, J. Searcy, E. Shabalina, K. Shaw, J. Sjolín, R. Soualah, S. Stamm, D. Ta, T. Theveniaux-Pelzer, E. Thompson, K. Uchida, L. Valery, M. Vreeswijk, C. Wasicki, I. Watson, K. Yau, J. Zhong, H. Zhu, and M. zur Nedden, *Object selection and calibration, background estimations and MC samples for the Winter 2013 Top Quark analyses with 2012 data*, Tech. Rep. ATL-COM-PHYS-2013-088, CERN, Geneva, Jan, 2013.
- [50] ATLAS Collaboration Collaboration, *Muon reconstruction efficiency in reprocessed 2010 LHC proton-proton collision data recorded with the ATLAS detector*, Tech. Rep. ATLAS-CONF-2011-063, CERN, Geneva, Apr, 2011.
- [51] G. P. Salam, *Towards Jetography*, Eur.Phys.J. **C67** (2010) 637–686, [arXiv:0906.1833 \[hep-ph\]](https://arxiv.org/abs/0906.1833).
- [52] M. Cacciari, G. P. Salam, and G. Soyez, *The anti- k_t jet clustering algorithm*, JHEP **04** (2008) 063, [arXiv:0802.1189v2 \[hep-ph\]](https://arxiv.org/abs/0802.1189v2).

- [53] M. Cacciari and G. P. Salam, *Dispelling the N^3 myth for the k_t jet-finder*, *Phys. Lett. B* **641** (2006) 57, [arXiv:0512210v2 \[hep-ph\]](#).
- [54] M. Cacciari, G. P. Salam, and G. Soyez, *FastJet User Manual*, *Eur. Phys. J. C* **72** (2012) 1896, [arXiv:1111.6097 \[hep-ph\]](#).
- [55] ATLAS Collaboration, *Jet energy measurement with the ATLAS detector in proton-proton collisions at $\sqrt{s} = 7$ TeV*, *Eur. Phys. J. C* **73** (2013) 2304, [arXiv:1112.6426 \[hep-ex\]](#).
- [56] C. Cojocaru et al., *Hadronic calibration of the ATLAS liquid argon end-cap calorimeter in the pseudorapidity region $1.6 < |\eta| < 1.8$ in beam tests*, *Nucl. Instr. Meth. A* **531** (2004) 481, [arXiv:0407009 \[physics\]](#).
- [57] T. Barillari et al., *Local hadronic calibration*, ATL-LARG-PUB-2009-001 (2009) . <https://cds.cern.ch/record/1112035>.
- [58] ATLAS Collaboration, *Commissioning of the ATLAS high-performance b-tagging algorithms in the 7 TeV collision data*, ATLAS-CONF-2011-102 (2011) . <https://cds.cern.ch/record/1369219>.
- [59] ATLAS Collaboration, *Measurement of the b-tagging efficiency in a sample of jets containing muons with 5 fb^{-1} of data from the ATLAS detector*, ATLAS-CONF-2012-043 (2012) . <https://cdsweb.cern.ch/record/1435197>.
- [60] ATLAS Collaboration, *Performance of Missing Transverse Momentum Reconstruction in Proton-Proton Collisions at 7 TeV with ATLAS*, *Eur. Phys. J. C* **72** (2012) 1844, [arXiv:1108.5602 \[hep-ex\]](#).
- [61] J. Aguilar-Saavedra, R. Benbrik, S. Heinemeyer, and M. Perez-Victoria, *A handbook of vector-like quarks: mixing and single production*, [arXiv:1306.0572 \[hep-ph\]](#).
- [62] ATLAS Collaboration, *Search for pair production of new heavy quarks that decay to a Z boson and a third generation quark in pp collisions at $\sqrt{s} = 8$ TeV with the ATLAS detector*, ATLAS-CONF-2013-056 (Jun, 2013) .
- [63] A. collaboration, *Search for anomalous production of events with same-sign dileptons and b jets in 14.3 fb^{-1} of pp collisions at $\sqrt{s} = 8$ TeV with the ATLAS detector*, .
- [64] P. Golonka and Z. Wąs, *PHOTOS Monte Carlo: a precision tool for QED corrections in Z and W decays*, *Eur. Phys. J. C* **45** (2006) 97, [arXiv:0506026 \[hep-ph\]](#).
- [65] S. Jadach, J. H. Kühn, and Z. Wąs, *TAUOLA - a library of Monte Carlo programs to simulate decays of polarized τ leptons*, *Comput. Phys. Commun.* **64** (1991) 275.
- [66] S. Frixione and B. R. Webber, *Matching NLO QCD computations and parton shower simulations*, *JHEP* **06** (2002) 029, [arXiv:0204244 \[hep-ph\]](#).
- [67] S. Frixione, E. Laenen, P. Motylinski, and B. R. Webber, *Single-top production in MC@NLO*, *JHEP* **03** (2006) 092, [arXiv:0512250 \[hep-ph\]](#).

- [68] S. Frixione, E. Laenen, P. Motylinski, C. White, and B. R. Webber, *Single-top hadroproduction in association with a W boson*, **JHEP** **07** (2008) 029, [arXiv:0805.3067 \[hep-ph\]](#).
- [69] H.-L. Lai et al., *New parton distributions for collider physics*, **Phys. Rev. D** **82** (2010) 074024, [arXiv:1007.2241 \[hep-ph\]](#).
- [70] M. Aliev et al., *HATHOR: a Hadronic Top and Heavy quarks cross section calculator*, **Comput. Phys. Commun.** **182** (2011) 1034, [arXiv:1007.1327 \[hep-ph\]](#).
- [71] A. D. Martin et al., *Uncertainties on α_S in global PDF analyses and implications for predicted hadronic cross sections*, **Eur. Phys. J. C** **64** (2009) 653, [arXiv:0905.3531 \[hep-ph\]](#).
- [72] P. M. Nadolsky et al., *Implications of CTEQ global analysis for collider observables*, **Phys. Rev. D** **78** (2008) 013004, [arXiv:0802.0007 \[hep-ph\]](#).
- [73] M. L. Mangano et al., *Multijet matrix elements and shower evolution in hadronic collisions: $Wb\bar{b} + n$ jets as a case study*, **Nucl. Phys. B** **632** (2002) 343, [arXiv:0108069 \[hep-ph\]](#).
- [74] ATLAS Collaboration, *Measurement of the t -channel single top-quark production cross section in pp collisions at $\sqrt{s} = 7$ TeV with the ATLAS detector*, **Phys. Lett. B** **717** (2012) 330, [arXiv:1205.3130 \[hep-ex\]](#).
- [75] K. Melnikov and F. Petriello, *Electroweak gauge boson production at hadron colliders through $\mathcal{O}(\alpha_s^2)$* , **Phys. Rev. D** **74** (2006) 114017, [arXiv:0609070 \[hep-ph\]](#).
- [76] ATLAS Collaboration, *Measurement of the charge asymmetry in top quark pair production in pp collisions at $\sqrt{s} = 7$ TeV using the ATLAS detector*, **Eur. Phys. J. C** **72** (2012) 2039, [arXiv:1203.4211 \[hep-ex\]](#).
- [77] T. Sjostrand et al., *High-energy-physics event generation with Pythia 6.1*, **Comput. Phys. Commun.** **135** (2001) 238, [arXiv:0010017 \[hep-ph\]](#).
- [78] A. Sherstnev and R. Thorne, *Parton distributions for LO generators*, **Eur. Phys. J. C** **55** (2008) 553, [arXiv:0711.2473 \[hep-ph\]](#).
- [79] N. Kidonakis, *Next-to-next-to-leading-order collinear and soft gluon corrections for t -channel single top quark production*, **Phys. Rev. D** **83** (2011) 091503, [arXiv:1103.2792 \[hep-ph\]](#).
- [80] N. Kidonakis, *Next-to-next-to-leading logarithm resummation for s -channel single top quark production*, **Phys. Rev. D** **81** (2010) 054028.
- [81] J. M. Campbell and R. K. Ellis, *$t\bar{t}W$ production and decay at NLO*, [arXiv:1204.5678 \[hep-ph\]](#).
- [82] M. V. Garzelli, A. Kardos, C. G. Papadopoulos, and Z. Trsyi, *$t\bar{t}W$ and $t\bar{t}Z$ Hadroproduction at NLO accuracy in QCD with Parton Shower and Hadronization effects*, **JHEP** **1211** (2012) 056, [arXiv:1208.2665 \[hep-ph\]](#).

- 1660 [83] LHC Higgs Cross Section Working Group Collaboration, S. Dittmaier et al., *Handbook*
1661 *of LHC Higgs Cross Sections: 1. Inclusive Observables*, [arXiv:1101.0593 \[hep-ph\]](#).
- 1662 [84] J. Campbell and R. Ellis, *An update on vector boson pair production at hadron*
1663 *colliders*, *Phys. Rev. D* **60** (1999) 113006, [arXiv:9905386 \[hep-ph\]](#).
- 1664 [85] J. A. Aguilar-Saavedra, *Identifying top partners at LHC*, *JHEP* **11** (2009) 030,
1665 [arXiv:0907.3155 \[hep-ph\]](#).
- 1666 [86] J. A. Aguilar-Saavedra, *PROTOS, a Program for Top Simulations*, .
1667 <http://jaguar.web.cern.ch/jaguar/protos/>.
- 1668 [87] A. Djouadi, J. Kalinowski, and M. Spira, *HDECAY: a Program for Higgs Boson*
1669 *Decays in the Standard Model and its Supersymmetric Extension*,
1670 *Comput. Phys. Commun.* **108** (1998) 56, [arXiv:9704448 \[hep-ph\]](#).
- 1671 [88] ATLAS Collaboration, *Measurement of the top quark-pair production cross section*
1672 *with ATLAS in pp collisions at $\sqrt{s} = 7$ TeV*, *Eur. Phys. J. C* **71** (2011) 1577,
1673 [arXiv:1012.1792 \[hep-ex\]](#).

